

**ACTIVE CONTROL OF VIBRATIONS TRANSMITTED THROUGH  
A CAR SUSPENSION**

**Jean-Gabriel Roumy**

Department of Electrical and Computer Engineering  
McGill University, Montreal

August 2003

A thesis submitted to McGill University in partial fulfilment of the requirements for the  
degree of Master of Engineering

© Jean-Gabriel Roumy, MMIII

## ABSTRACT

The vibrations caused by road imperfections, which are transmitted to a car frame through the suspension, are one of the major sources of ambient noise inside the passenger compartment of an automobile.

A solution to this problem is the addition of feedback-controlled actuators between the suspension attachment points and the car frame. These actuators can be driven to provide an active control of the vibrations, thus reducing greatly the magnitude of the forces exerted on the car frame at the suspension attachment points. In order to implement a robust yet effective controller, a model of a  $\frac{1}{4}$  car suspension (suspension associated to a single wheel) is derived from experimentally acquired data. The structure's modal parameters are extracted from Frequency Response data, and are used to obtain a state-space realization. The performance of controller design techniques such as LQR and  $H_\infty$  is assessed through simulation using the model of the suspension.

## RÉSUMÉ

Les vibrations causées pas les imperfections de la route et transmises au châssis d'une automobile à travers la suspension sont une cause majeure de bruit ambiant à l'intérieur du compartiment passager.

Une solution à ce problème est l'ajout d'actionneurs entre les points d'ancrage de la suspension et le châssis. Ces actionneurs permettent d'exercer une ~~contrôle-commande~~ actif-active des vibrations, réduisant de façon significative l'amplitude des forces exercées sur le châssis de l'automobile aux points d'ancrage de la suspension. Afin ~~d'implémenter d'implanter~~ un ~~contrôleur-compensateur~~ robuste et performant, un modèle d'un quart de suspension automobile (suspension associée ~~a-à~~ une seule roue) est ~~dérivé~~ obtenu à partir de données acquises expérimentalement. Les paramètres modaux de la structure sont calculés à partir de données de réponse en fréquence, et sont utilisés pour obtenir une réalisation du modèle. La performance d'algorithmes de ~~contrôle-commande~~ tels LQR et  $H_\infty$  est évaluée par simulation du modèle. [[note: contrôle est un anglicisme]]

## ACKNOWLEDGEMENTS

...

# Table of Contents

<b>LIST OF FIGURES .....</b>	<b>VI</b>
<b>LIST OF TABLES .....</b>	<b>IX</b>
<b>GLOSSARY OF ACRONYMS.....</b>	<b>X</b>
<b>1 INTRODUCTION.....</b>	<b>1</b>
1.1 OBJECTIVE .....	1
1.2 THESIS OUTLINE.....	2
<b>2 LITERATURE REVIEW.....</b>	<b>3</b>
<b>3 MODEL IDENTIFICATION.....</b>	<b>6</b>
3.1 MODAL TESTING.....	6
3.2 EXPERIMENTAL DATA ACQUISITION .....	6
3.2.1 <i>Raw Data Acquisition</i> .....	6
3.2.2 <i>FRF computation</i> .....	8
3.2.3 <i>Data Selection</i> .....	10
3.3 MODAL PARAMETERS IDENTIFICATION .....	12
3.3.1 <i>Curve Fitting</i> .....	12
3.3.2 <i>FRF Transfer Function</i> .....	12
3.3.3 <i>Degrees of Freedom Identification</i> .....	14
3.3.4 <i>Curve Fitting Algorithm</i> .....	16
3.3.5 <i>Curve Fitting Results</i> .....	18
3.4 STATE SPACE REALIZATION .....	25
3.5 MODEL DISCRETIZATION .....	29
3.6 NON-COLLOCATED ACTUATOR.....	32
3.7 MODEL LIMITATIONS .....	34
3.8 SYSTEM SIMULATION .....	35
<b>4 CONTROLLER DESIGN .....</b>	<b>38</b>
4.1 STATE-FEEDBACK REGULATOR DESIGN .....	38

4.2	KALMAN FILTER .....	39
4.2.1	<i>Design</i> .....	39
4.2.2	<i>Results</i> .....	42
4.3	LQR CONTROLLER DESIGN.....	45
4.4	$H_\infty$ CONTROLLER DESIGN .....	<del>46</del> 45
4.5	CLOSED-LOOP SYSTEM RESULTS.....	48
4.5.1	<i>LQR regulator, collocated actuator</i> .....	48
4.5.2	<i>LQR regulator, non-collocated actuator</i> .....	<del>56</del> 55
4.5.3	<i><math>H_\infty</math> controller, collocated actuator</i> .....	<del>60</del> 59
<b>5</b>	<b>CONCLUSION</b> .....	<del>66</del> 65
5.1	SUMMARY .....	<del>66</del> 65
5.2	FUTURE WORK.....	<del>67</del> 66

# List of Figures

Figure 1 - Experimental test bench at Université de Sherbrooke.....	7
Figure 2 - Sensor location on the suspension.....	8
Figure 3 - Sample FRF showing H, H1 and H2.....	11
Figure 4 - Sample Coherence function.....	11
Figure 5 - Sum of the acceleration/force FRFs.....	15
Figure 6 - Sum of the force/force FRFs.....	15
Figure 7 - Fit performed on the FRF taken at b1, x direction.....	19
Figure 8 - Fit performed on the FRF taken at bh, z direction.....	20
Figure 9 – Second fit performed on the FRF taken at b1, x direction.....	23
Figure 10 - Second fit performed on the FRF taken at b1, y (left) and b1, z (right).....	23
Figure 11 - Second fit performed on the FRF taken at bh, z direction.....	24
Figure 12 - Second fit performed on the FRF taken at bh, x (left) and bh, y (right).....	25
Figure 13 – Zero-order hold discretization method.....	29
Figure 14 – Comparison of continuous-time and discrete-time bode plots.....	31
Figure 15 – Pole-zero plot of the discrete-time state space model.....	32
Figure 16 – bh-x receptance FRF, actuator non-collocated.....	33
Figure 17 – bh-y receptance FRF, actuator non-collocated.....	33
Figure 18 – bh-z receptance FRF, actuator non-collocated.....	34
Figure 19 – Simulink simulation of discrete model.....	35
Figure 20 – FFT of white noise disturbance.....	36
Figure 21 – FRFs taken from the b1 attachment point, x direction output.....	37
Figure 22 – Regulator implementation with a collocated actuator.....	38
Figure 23 - Regulator implementation with a non-collocated actuator.....	39
Figure 24 – Output Signal and noise magnitude comparison for the b1, x direction sensor .....	39
Figure 25 – Kalman Filter implementation.....	41
Figure 26 – Regulator including Kalman filter.....	<a href="#">4241</a>
Figure 27 – Sample filter gain convergence.....	<a href="#">4342</a>

Figure 28 – First state true value (left) and estimated value (right).....	43
Figure 29 – error on the first state.....	<a href="#">4443</a>
Figure 30 – Second state true value (left) and estimated value (right) .....	44
Figure 31 – Error on the second state.....	<a href="#">4544</a>
Figure 32 - $H_\infty$ system configuration.....	46
Figure 33 - b1, x direction closed-loop dB attenuation (true states, collocated actuator) .....	<a href="#">4948</a>
Figure 34 - b1, y (left) and b1, z (right) closed-loop dB attenuation (true states, collocated actuator).....	49
Figure 35 - bh, z direction closed-loop dB attenuation (true states, collocated actuator) .....	<a href="#">5049</a>
Figure 36 - bh, x (left) and bh, y (right) closed-loop dB attenuation (true states, collocated actuator).....	50
Figure 37 – Disturbance (left) and control signal (right) amplitude .....	<a href="#">5150</a>
Figure 38 – b1, x direction closed-loop dB attenuation (estimated states, collocated actuator).....	<a href="#">5251</a>
Figure 39 – b1, y (left) and b1, z (right) closed-loop dB attenuation (estimated states, collocated actuator).....	52
Figure 40 - bh, z direction closed-loop dB attenuation (estimated states, collocated actuator).....	<a href="#">5352</a>
Figure 41 - bh, x (left) and bh, y (right) closed-loop dB attenuation (estimated states, collocated actuator).....	<a href="#">5352</a>
Figure 42 - b1, x direction FRF with emphasis on reducing high-frequency peaks .....	<a href="#">5453</a>
Figure 43 - b1, y (left) and b1, z (right) FRF with emphasis on reducing high-frequency peaks.....	<a href="#">5554</a>
Figure 44 - bh, z direction FRF with emphasis on reducing high-frequency peaks .....	<a href="#">5554</a>
Figure 45 - bh, x (left) and bh, y (right) FRF with emphasis on reducing high-frequency peaks.....	<a href="#">5655</a>
Figure 46 – Comparison of the effect of actuator placement, bh – z direction sensor..	<a href="#">5756</a>
Figure 47 – b1, x direction closed-loop dB attenuation (estimated states, non-collocated actuator).....	<a href="#">5857</a>

Figure 48 – b1, y (left) and b1,z (right) closed-loop dB attenuation (estimated states, non-collocated actuator).....	<a href="#">5857</a>
Figure 49 – bh, z direction closed-loop dB attenuation (estimated states, non-collocated actuator).....	<a href="#">5958</a>
Figure 50 – bh, x (left) and bh, y (right) closed-loop dB attenuation (estimated states, non-collocated actuator).....	<a href="#">5958</a>
Figure 51 – b1, x direction closed-loop dB attenuation ( $H_\infty$ controller).....	<a href="#">6160</a>
Figure 52 – b1, y (left) and b1, z (right) direction closed-loop dB attenuation ( $H_\infty$ controller).....	<a href="#">6160</a>
Figure 53 - bh, z direction closed-loop dB attenuation ( $H_\infty$ controller).....	<a href="#">6261</a>
Figure 54 - bh, x (left) and bh, y (right) direction closed-loop dB attenuation ( $H_\infty$ controller).....	<a href="#">6261</a>
Figure 53 – b1, x direction closed-loop dB attenuation on randomized model ( $H_\infty$ controller).....	<a href="#">6362</a>
Figure 53 – b1, y (left) and b1, z (right) direction closed-loop dB attenuation on randomized model ( $H_\infty$ controller).....	<a href="#">6362</a>
Figure 57 – bh, z direction closed-loop dB attenuation on randomized model ( $H_\infty$ controller).....	<a href="#">6463</a>
Figure 58 – bh, x (left) and bh, y (right) direction closed-loop dB attenuation on randomized model ( $H_\infty$ controller).....	<a href="#">6463</a>

# List of tables

Table 1 - Preliminary identified resonance modes.....	16
Table 2 - b1-x fit results and statistics.....	20
Table 3 - bh-z fit results and statistics.....	21
Table 4 - modes of vibration of the $\frac{1}{4}$ car suspension.....	22
Table 5 - b1-x second fit statistics.....	23
Table 6 - b1, y (left) and b1, z (right) second fit statistics .....	24
Table 7 - bh-z second fit statistics.....	24
Table 8 - bh-x (left) and b1, y (right) second fit statistics.....	25

# Glossary of Acronyms

<b>DOF</b> :	Degrees Of Freedom
<b>FEM</b> :	Finite Element Model
<b>FFT</b> :	Fast Fourier Transform
<b>FRF</b> :	Frequency Response Function
<b>LQR</b> :	Linear Quadratic Regulator
<b>MAC</b> :	Modal Assurance Criterion
<b>MDOF</b> :	Multiple Degrees Of Freedom
<b>MIMO</b> :	Multiple-Input, Multiple-Output
<b>RMSE</b> :	Root Mean Squared Error
<b>RT</b> :	Real-Time
<b>SDOF</b> :	Single Degree Of Freedom
<b>SISO</b> :	Single-Input, Single-Output
<b>SS</b> :	State Space
<b>SVD</b> :	Singular Value Decomposition
<b>ZOH</b> :	Zero-Order Hold

---

# 1 Introduction

## 1.1 Objective

There has been much talk lately about reducing polluting emissions from automobiles to preserve the environment. However, toxic gases are not the only kind of pollution emitted by vehicles; noise is another form of pollution, creating an uncomfortable environment for both those outside and inside the automobile. The aim of this thesis is to demonstrate a means of reducing the noise level inside the passenger compartment of an automobile thus making the ride more enjoyable for the occupants.

There are many sources that can generate noise inside a vehicle. The principal sources are the engine, the air ducts and the vibrations transmitted to the car frame. There has already been much work done in order to reduce the engine noise level, such as soundproofing the engine compartment and soft mounting the engine to reduce the vibrations transmitted to the car frame. The air ducts also produce a fair level of noise inside the passenger compartment. However, the principal sources of low-frequency noise are the vibrations caused by the road imperfections that are transmitted to the car frame through the suspension.

While most of today's car suspension systems are tuned so as to give good handling characteristics while maintaining a smooth ride ("douceur de roulement"), road imperfections create relatively low-frequency vibrations (below 200 Hz) that are not damped efficiently by passive suspension components (shocks, springs, rubber mats) and are transmitted to the car frame.

One solution to this problem is the addition of feedback-controlled actuators between the suspension attachment points and the car frame. These actuators can be driven to provide an active control of the vibrations, thus reducing greatly the magnitude of the forces exerted on the car frame at the suspension attachment points. The objectives

of this thesis are to derive a model of a  $\frac{1}{4}$  car suspension (suspension associated to a single wheel) from experimentally acquired data, and design a feedback controller for the actuators in order to reduce vibrations.

## 1.2 Thesis Outline

The design of a robust and effective feedback controller requires an accurate model of the plant being controlled. Therefore, it is necessary to construct a model of a car suspension to simulate its dynamics. Using experimental data from a  $\frac{1}{4}$  car suspension test bench, Frequency Response Functions (FRFs) are computed from which the structure's vibration characteristics are extracted through a process called curve fitting. Curve fitting consists in identifying the parameters of a transfer function corresponding to the FRF. Once these parameters are known, a model is derived in the form of a State Space realization.

With an accurate model available, the actual controller design can start. Since the system's states are not directly observable, a Kalman filter is used in order to reconstruct the states from the outputs. The controller then uses the state estimates as if they were the true states. An LQR regulator is designed, although it is not very robust to modeling errors. In order to account for the model uncertainty, a robust  $H_\infty$  controller is then designed for the actuators using the reworked model. The  $H_\infty$  design algorithm adds a certain measure of uncertainty to the model when computing the controller gains, which results in a more robust design.

---

## 2 Literature Review

There has already been some work done in order to identify the sources of noise inside the passenger compartment of an automobile and implement solutions to reduce it. The solutions can range from passive means of increasing damping to active control of vibrations, or an entirely different approach where an active noise control algorithm is developed.

Hermans and Van Der Auweraer [1] have analysed the sources of ambient noise by taking structural and acoustical measurements inside an automobile under operating conditions. They noticed a booming noise problem occurred at a frequency of 80Hz, and this frequency remained constant during road tests at different speeds and engine RPMs. The amplitude of the response, however, varied with the road surface. It thus confirmed the road-induced nature of the noise, and the “booming” was related to a resonance. By combining operational and laboratory FRF measurements, a transmission path was found, which showed that the rear suspension mounts were dominantly contributing in this frequency range.

Similarly, Kim, Lee and Sung [2] found that car interior noise is caused in the low-frequency range by modal characteristics of the structure such as acoustic resonances, body vibration modes and structural-acoustic coupling characteristics. A noise analysis and reduction scheme, assisted by experiments, is introduced in which the experimental modal data is used in numerical analysis. For a medium-sized car, 8 acoustic modes are calculated and measured below 200 Hz. In the same frequency range, 20 structural modes are measured using experimental modal analysis. To find the dominant structural and acoustic modes involved in noise peaks, the structural-acoustic modal coupling coefficients are calculated. To reduce the dominant coupling coefficients, commercial damping sheet (asphalt pad) is attached on the front floor of the test automobile, which is identified as the source of the most sensitive dominant coupling coefficients. A significant reduction is observed in the large coefficient, and the resulting increase in structural damping lessens the resonance effect and results in a drop in noise

level. A reduction of about 5 dB in the sound pressure level as measured at the driver position is observed after the damping treatment.

Stobener and Gaul [3], on the other hand, have chosen to extend the application of modal control concepts to structures with complex geometries. Since the evaluation of modal parameters for such structures through numerical computations of local modes is complex, an experimental modal analysis is performed. The car body of a modern roadster is used to perform the tests, and an array of piezoelectric sensors and actuators is placed on the floor and center panels. The FRFs are computed and the modal parameters extracted through curve fitting, revealing 11 vibration modes for the centre panel and 8 for the floor panel. The modal input and output matrices are derived in the form of a modal state-space formulation which is standard in modern control theory. Using this model, the control law is formulated in modal coordinates. The gain factors of the feedback loop correspond directly to the natural frequencies and modal damping ratios of the system matrix and can therefore be chosen to change the modal damping ratios and eigenfrequencies of the controlled system in a specified way. To conduct an experimental test, collocated sensors and actuators are not necessary since the sensor inputs are filtered to achieve modal displacements and velocities. A reduction of between 25% and 60 % is achieved on the resonance peaks, as measured with accelerometers, depending on the actuator placement.

The  $H_\infty$  control design technique, being robust to model uncertainties and parameter variations, represents an interesting option when implementing a modal controller, as demonstrated by Kar, Seto and Doi in [4]. They present the experimental results of a robust control scheme to suppress the vibrations of a flexible structure. First, a 5 DOF model of a flexible bridge tower connected with a crane structure is derived using numerical analysis and FEM. The reduced-order model created neglects the high frequency modes, thus creating some uncertainty. A feedback controller is designed using the  $H_\infty$  based control theory and is tested in simulation and on the real structure. The controller is able to suppress the low-order vibration modes without any spillover

instability due to the neglected modes. Furthermore, the controller is also shown to be robust against variations of the model parameters.

An entirely different method to limit the sound level in an automobile, as described by Elliott in [5], involved using loudspeakers to implement an active control of structure-borne noise. The control of sound in an enclosure can be achieved by minimizing the total acoustic potential energy in the enclosure. To do so, secondary acoustic sources are adjusted in amplitude and phase to minimize the acoustic energy in the enclosure. An adaptive feedforward controller is described for the control of engine and road noise in cars. In this approach, a separate reference signal is used to drive the secondary source. This reference signal must be well correlated with the signal from the primary source. Therefore, the control filters must adapt to changes in excitation due, for example, to the changing car speed. To do so, they must model a broadband response. A reduction of 10 dB in the noise amplitude as measured at the front of the car can be achieved using this method.

---

# 3 Model Identification

## 3.1 Modal testing

Modal testing is a good way of accurately modelling a complex structure. It also provides a mean of correlating the experimental data with a numerical model such as a Finite Element Model. Modal representation describes the system in terms of its dynamic properties, or modes of vibration. A mechanical structure exhibits a different level of response to an applied force that is constant in amplitude, but whose rate of oscillation varies. A mode of vibration exists when the structure exhibits a strong response, called a resonance, to a sinusoidal input. A structure may have several modes of vibration and each is characterised by its undamped natural frequency and damping ratio. The equation representing a single mode of vibration is

$$H(s) = \frac{A}{s^2 + 2\zeta\omega_n s + \omega_n^2} \quad (1)$$

Where  $A$  is the gain,  $\zeta$  is the damping ratio and  $\omega_n$  is the undamped natural frequency. The resonance frequency, which gets very close to  $\omega_n$  at low damping ratios, is given by

$$\omega_r = \omega_n \sqrt{1 - 2\zeta^2} \quad (2)$$

The natural frequencies and damping ratios are particular to a structure and do not change depending on the output sensor placement, but the amplitude of the response varies according to where the sensor is located. Modal testing is accomplished by exciting a structure with an input simulating a disturbance (either using a shaker or by impact testing) and recording the system's behaviour (displacement, force, velocity or acceleration).

## 3.2 Experimental Data Acquisition

### 3.2.1 Raw Data Acquisition

An accurate model is necessary if good performance is to be expected from a controller. In the case of a car suspension, a traditional Finite Element Model (FEM) would be computationally expensive, and would yield poor results in view of the complexity of the structure without a way to correlate it to the real structure. Therefore, a more accurate model in this case is obtained using experimentally acquired data from a real car suspension.

To this end, researchers from the GAUSS laboratory at Université de Sherbrooke set up a  $\frac{1}{4}$  car suspension test bench. They used this test bench to perform a frequency analysis on the complete suspension from which they obtained all the FRFs necessary to derive a model. [6]

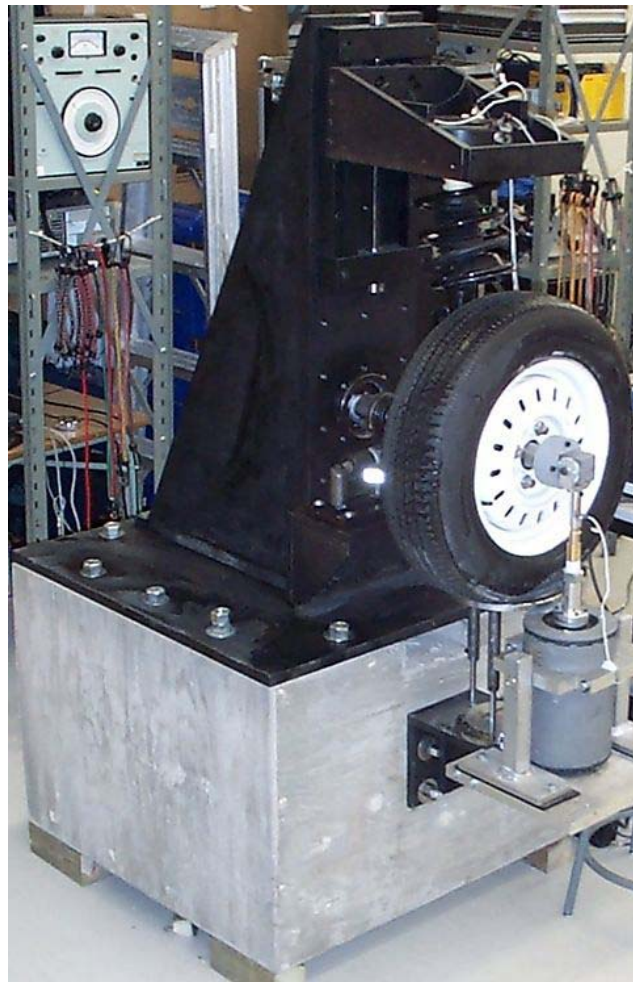


**Figure 1 - Experimental test bench at Université de Sherbrooke**

Figure 1~~Figure-1~~ shows the experimental test bench. A shaker is attached to the wheel axle to simulate the disturbance. A force sensor records the force applied to the axle. Different acceleration and force sensors are placed on the suspension attachment points to record its behavior when excited.

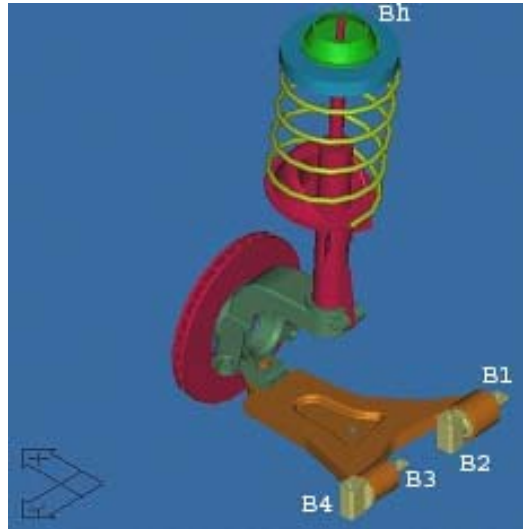


**Figure 2 - Sensor location on the suspension**

Figure 2~~Figure-2~~ shows the location and denomination of the suspension attachment points to the car frame. Four 3-axis (x, y and z) accelerometers are placed at the suspension base's attachment points (B1, B2, B3 and B4). Three force sensors are placed at the head of the suspension (Bh) to record its behavior in all three axes. The suspension is excited through the shaker with white Gaussian noise for a period of 6 seconds during which sensor information is recorded at a sampling frequency of 1000 Hz. The type of force sensor used gives a value that is proportional to the displacement of the structure, as the force exerted is the recorded displacement times a constant.

### **3.2.2 FRF computation**

A frequency analysis is performed on the raw data to derive the FRFs for all 15 outputs. The FRFs describe the system's behavior in the frequency domain.

The computation of the FRFs relies on the following equations, which relate the excitation and the response of a system:

$$\begin{aligned}
S_{xx}(\omega) &= |H(\omega)|^2 \cdot S_{ff}(\omega) \\
S_{fx}(\omega) &= H(\omega) \cdot S_{ff}(\omega) \\
S_{xx}(\omega) &= H(\omega) \cdot S_{xf}(\omega)
\end{aligned}
\tag{3}$$

Where

$S_{fx}(\omega)$  is the cross-spectrum of excitation and response

$S_{ff}(\omega)$  is the auto-spectrum of the excitation

$S_{xx}(\omega)$  is the auto-spectrum of the response

$S_{xf}(\omega)$  is the cross spectrum of response and excitation

$H(\omega)$  is the FRF linking the output and the input

[[it would be worthwhile to give the formulas to compute auto- and cross-spectra]]

The FRFs are computed using more than one of the previous equations, providing a crosscheck of the results [7, 8, 9].

$$\begin{aligned}
H_1(\omega) &= \frac{S_{fx}(\omega)}{S_{ff}(\omega)} \\
H_2(\omega) &= \frac{S_{xx}(\omega)}{S_{xf}(\omega)}
\end{aligned}
\tag{4}$$

In theory,  $H_1(\omega)$  and  $H_2(\omega)$  should be identical. However, they will differ due to physical constraints such as noise on the input or the output sensor signal, nonlinearities on the structure or finite sampling. The coherence value, defined as  $\gamma(\omega)^2$ , provides a means of quantifying the uncertainty on the FRFs.

$$\gamma(\omega)^2 = \frac{H_1(\omega)}{H_2(\omega)} = \frac{|S_{fx}^2(\omega)|}{(S_{ff}(\omega)S_{xx}(\omega))}
\tag{5}$$

The coherence is always less than or equal to 1.0. A value inferior to 1.0 means that there is a discrepancy between  $H_1(\omega)$  and  $H_2(\omega)$ . Near a resonance, the input signal is likely to be influenced so  $S_{ff}(\omega)$  becomes uncertain, while near an antiresonance the response signal will be influenced making  $S_{xx}(\omega)$  uncertain. Therefore, near a resonance,  $H_2(\omega)$  is likely more accurate, while  $H_1(\omega)$  is a better approximation of the system response around an antiresonance. Generally, a coherence above 0.9 is considered good.

### 3.2.3 Data Selection

As mentioned in the previous section,  $H_2(\omega)$  represents the system more accurately around resonances while  $H_1(\omega)$  represents the system better around antiresonances. Since the aim is to control the vibrations transmitted through the suspension (reducing the amplitude of the resonance peaks), a model that is accurate in the vicinity of the system's resonant frequencies is more desirable. Thus,  $H_2(\omega)$  represents a better choice of data.

The sampling frequency used to acquire data on the experimental test bench is 1000 Hz. Therefore, from the sampling theorem, the FRFs represent the system behaviour up to 500 Hz. [Figure 3](#) represents the  $H$ ,  $H_1$  and  $H_2$  FRFs [\[\[What does H represent here? An FFT?\]\]](#) computed from the data of the x-direction accelerometer placed at B1. The coherence in this case degenerates below 20 Hz and above 250 Hz, as can be seen in [Figure 4](#). While not identical, the coherence functions for the other 14 outputs show the same trend. Furthermore, the resonance peaks present between 160 Hz and 250 Hz are generated by the tire, and thus are not considered in the model of the suspension, while the peaks below 160 Hz are generated by the dynamical properties of the suspension. Also considering that the low-frequency peaks generate the most noise inside the passenger compartment, and the pass band of the shaker, the frequency range of interest is chosen to be between 20 Hz and 160 Hz.

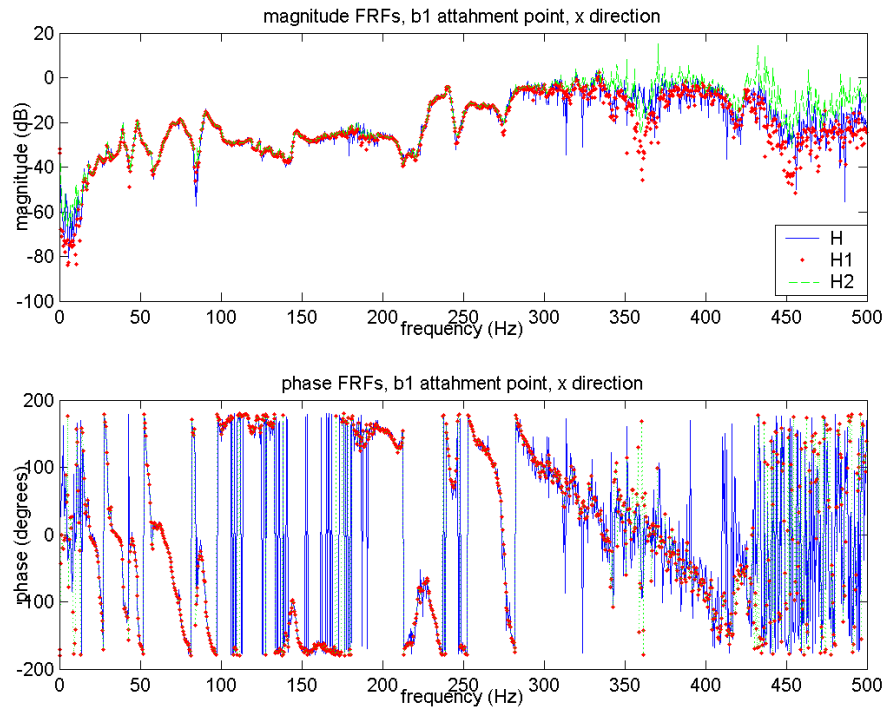


**Figure 3 - Sample FRF showing H, H1 and H2**

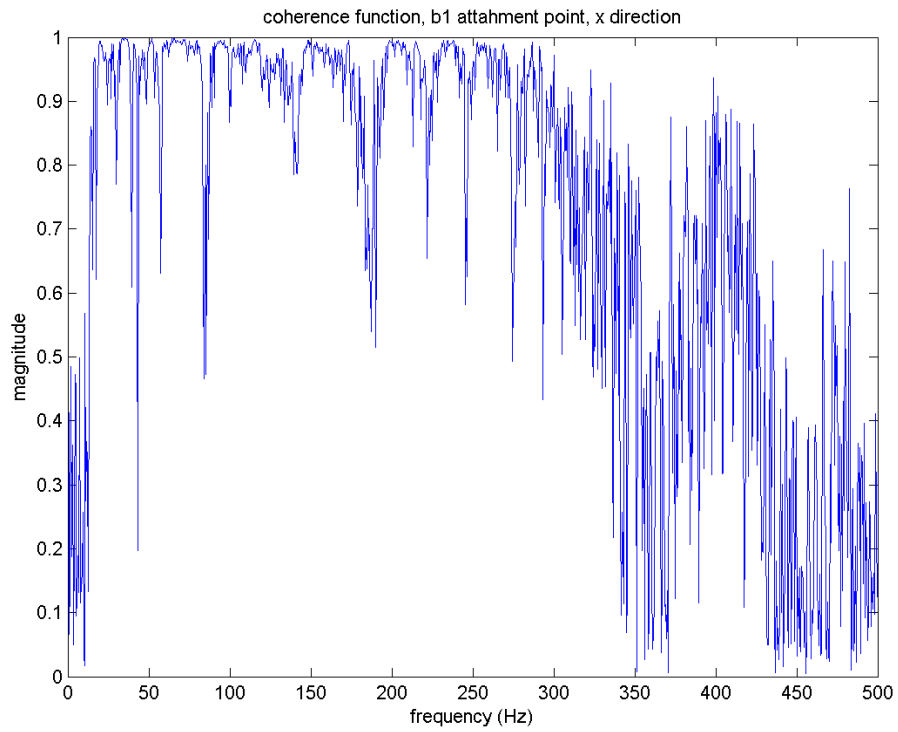


**Figure 4 - Sample Coherence function**

## 3.3 Modal Parameters Identification

### 3.3.1 Curve Fitting

Curve fitting is the process through which the model's modal parameters are determined. This procedure consists in fitting a theoretical equation to the experimental FRF data. This equation must be a rational transfer function for a finite dimensional state space realization to exist. The modal parameters sought are the transfer function coefficients that most closely approximate the measured data. There are several methods of curve fitting, and they can be categorized either as Single Degree of Freedom (SDOF) or Multiple Degrees of Freedom (MDOF).

SDOF methods, such as peak-picking or circle-fit, are used to separately identify the parameters of each resonant peak of an FRF, combining them afterwards in an effort to regenerate the FRF. These methods rely on the assumption that in the vicinity of a resonance the total response is dominated by the contribution of the mode whose natural frequency is closest. While these methods may work for systems which resonances are far apart, they are in general not very accurate and produce disappointing results on systems with many resonances in a small frequency range, or with very lightly damped modes.

MDOF methods on the other hand try to fit an equation to the whole FRF. The advantage of such methods is that the effect of one resonance on the neighbouring peaks is taken into consideration when closely coupled modes are present. The method implies finding simultaneously all the parameters of the transfer function describing a particular FRF.

### 3.3.2 FRF Transfer Function

There are ~~3~~three usual types of FRFs, described as the receptance, mobility and accelerance FRFs. The receptance is computed using the displacement as the output over

the force as the input, the mobility using velocity over force and the acceleration using acceleration over force [7, 9].

A single mode of vibration can be modeled in a receptance FRF as

$$H(\omega) = \frac{X(\omega)}{F(\omega)} = \frac{A}{\omega_n^2 - \omega^2 + 2j\zeta\omega_n\omega} \quad (6)$$

The equivalent mobility equation is

$$H(\omega) = \frac{V(\omega)}{F(\omega)} = \frac{Aj\omega}{\omega_n^2 - \omega^2 + 2j\zeta\omega_n\omega} \quad (7)$$

The equivalent acceleration equation is

$$H(\omega) = \frac{A(\omega)}{F(\omega)} = \frac{-A\omega^2}{\omega_n^2 - \omega^2 + 2j\zeta\omega_n\omega} \quad (8)$$

Where  $X(\omega)$  is the displacement output,  $V(\omega)$  is the velocity output,  $A(\omega)$  is the acceleration output,  $F(\omega)$  is the force input,  $\omega_n$  is the undamped natural frequency,  $\zeta$  is the damping ratio and  $A$  is the gain.

The FRFs measured at the base of the suspension are acceleration over force, therefore they are acceleration FRFs. The FRFs measured at the head of the suspension are force over force, but as mentioned earlier in this case the force output is proportional to the displacement, therefore these FRFs can be considered as receptance FRFs and the receptance equation can be used to model them.

Vibrating structures are conveniently represented by a parallel interconnection of the second-order transfer functions described in equations ~~(6)-(6)~~, ~~(7)-(7)~~ and ~~(8)-(8)~~. Therefore, an  $n$ -DOF FRFs can be modeled using the equations:

$$H(\omega) = \sum_{i=1}^n \frac{-A_i\omega^2}{\omega_{ni}^2 - \omega^2 + 2j\zeta_i\omega_{ni}\omega} \quad (9)$$

for an acceleration FRF and

$$H(\omega) = \sum_{i=1}^n \frac{A_i}{\omega_{ni}^2 - \omega^2 + 2j\zeta_i \omega_{ni} \omega} \quad (10)$$

for a receptance FRF.

The advantage of separating the transfer function into partial fractions is that the coefficients determined during the curve fitting process are directly related to the modal properties of the system. The number of members-terms in the summation (representing the Degrees of Freedom) is selected by visual inspection of the experimental FRFs. There must be enough DOFs to properly model all significant vibration modes of the structure, yet the model has to be of a low enough order so that it is manageable for numerical convenience.

### 3.3.3 Degrees of Freedom Identification

Since the resonance modes are characteristic of a structure and do not depend upon the sensor placement, all FRFs should exhibit the same resonance peaks albeit with different amplitudes. However, due to measurement noise or nonlinearities, the values of the resonance frequencies and damping ratios carry an uncertainty and can change slightly from one FRF to the other. Therefore, relying on a single FRF to identify the entire structure's modal parameters may lead to errors, either by the possible omission of a mode or by selecting a computational mode which is not a true characteristic of the structure. A solution to avoid these pitfalls is to plot the sum of all available FRFs. While the resulting FRF has no meaning, the real modes will tend to be amplified, as they are present on all FRFs, while the computational modes and the noise stay small, as they are different on each FRF. It is then easier to separate the real modes from the computational modes. However, since there are 2-two types of sensors (acceleration and force) and they have a very different scaling, the acceleration FRFs are added together and the force FRFs are added together, creating 2-two graphs from which to choose the structure's modes.

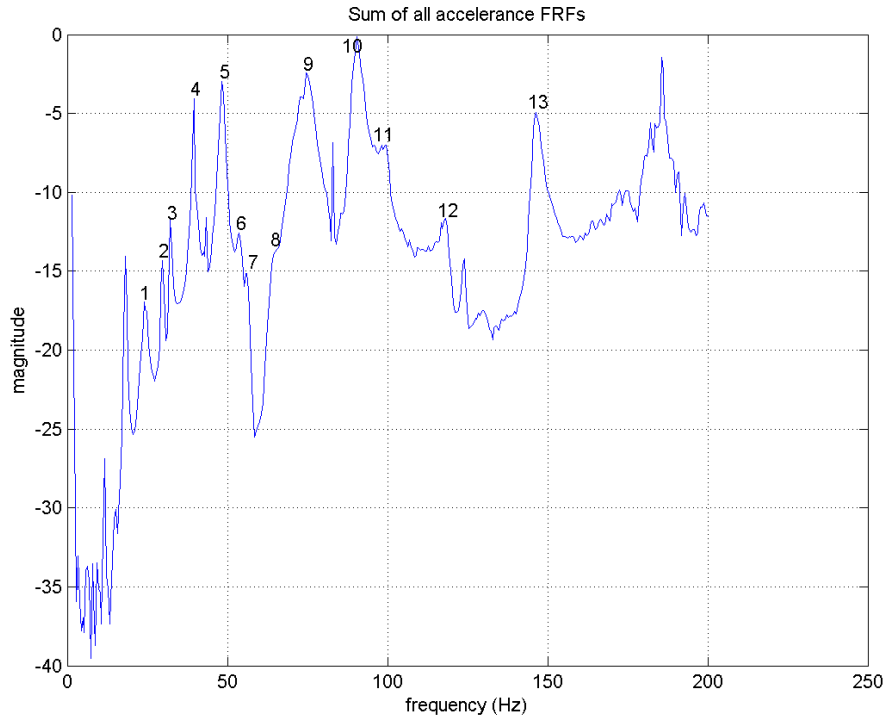


**Figure 55** - Sum of the acceleration/force FRFs

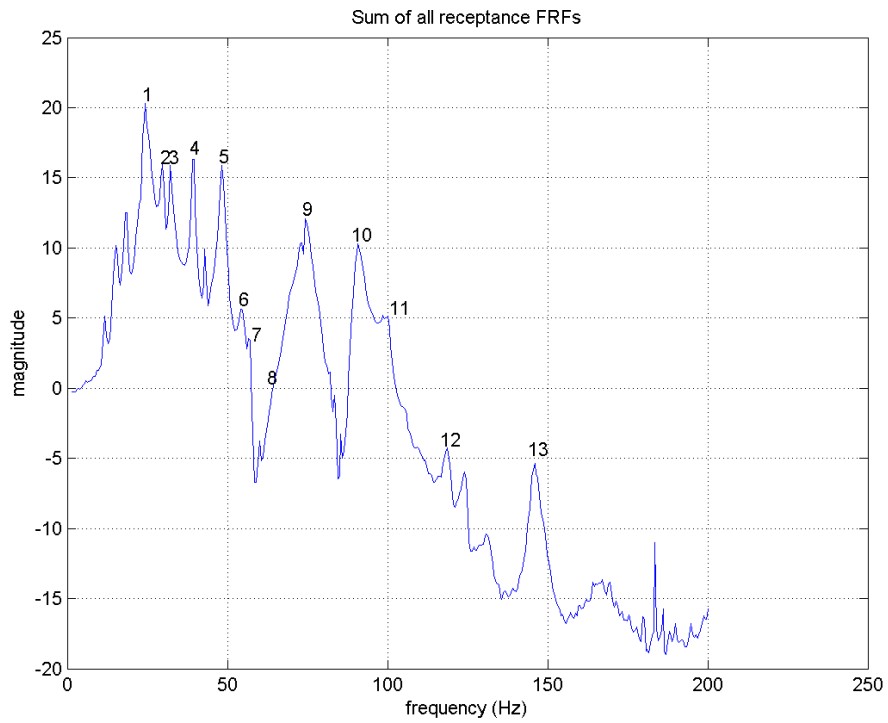


**Figure 66** - Sum of the force/force FRFs

As can be seen from [Figure 5](#) and [Figure 6](#), the acceleration FRFs (all taken at the base of the suspension) have better defined modes at relatively higher frequencies, whereas the force FRFs (all taken at the head of the suspension) have clear modes at lower frequencies.

Despite adding all the FRFs, it can be shown that certain modes which appear real are not part of the structures, such as the peak around 83 Hz on [Figure 5](#). This peak can be traced to a single data point on one FRF and does not appear on any other FRF. After careful consideration of all the data available, it is possible to distinguish 13 modes in the frequency range 20Hz to 160 Hz :

Mode	Estimated Frequency (Hz)
1	24.2
2	30.0
3	32.0
4	40.0
5	48.5
6	54.0
7	56.6
8	63.5
9	75.0
10	90.0
11	100.0
12	118.0
13	146.0

**Table 1 - Preliminary identified resonance modes**

### 3.3.4 Curve Fitting Algorithm

Once the resonance modes are estimated, a transfer function equation is fitted to each of the FRFs. The Matlab Curve Fitting toolbox is used to find the transfer function parameters that most closely approximate the FRFs. The toolbox uses least squares algorithms to deduce the parameters, a brief introduction to which follows.

The fitting process requires a model that relates the experimental data to the fitted data with one or more coefficients. The parameters computed are estimates of the “real” but unknown parameters. To obtain these estimates, the least squares method minimizes the summed square of residuals. A residual  $r_i$  for the  $i^{\text{th}}$  data point is the difference between the experimentally obtained value  $y_i$  and the fitted response value  $\tilde{y}_i$ , and represents the error associated with the data.

$$r_i = y_i - \tilde{y}_i \quad (11)$$

The Summed Squares of Residuals (or Sum of Squares Error) is given by

$$SSE = \sum_{i=1}^n r_i^2 = \sum_{i=1}^n w_i (y_i - \tilde{y}_i)^2 \quad (12)$$

Where  $n$  is the number of data points included in the fit and  $w_i$  is the weight (importance) accorded to the  $i^{\text{th}}$  data point.

The algorithm yielding the best results for fitting a transfer function to an FRF is the robust least squares using the Trust-region algorithm, the details of which are described in the Matlab Curve Fitting toolbox documentation [10].

There are several goodness of fit statistics provided in the Curve Fitting toolbox, among them are the R-square value and the Root Mean Squared Error. R-square measures how successful the fit is in explaining the variation of the data, and is the square of the correlation between the experimental values and the fitted values. It is defined as the ratio of the Sum of Squares of the Regression (SSR) and the Total Sum of Squares (SST). SSR is defined as :

$$SSR = \sum_{i=1}^n w_i (\tilde{y}_i - \bar{y})^2 \quad (13)$$

Where  $\bar{y}$  is the mean response value.

SST, also called the sum of squares about the mean, is defined as

$$SST = \sum_{i=1}^n w_i (y_i - \bar{y})^2 \quad (14)$$

Where  $SST = SSR + SSE$ . [\[\[I still don't see this. Prove it or give a ref\]\]](#)

Finally, R-square is expressed as

$$R - square = \frac{SSR}{SST} = 1 - \frac{SSE}{SST} \quad (15)$$

R-square can have a value between 0 and 1 and the higher the value, the better the fit.

Another indicator of the goodness of the fit is the RMSE value.

$$RMSE = \sqrt{MSE} = \sqrt{\frac{SSE}{v}} \quad (16)$$

Where MSE is the Mean Square Error and SSE is as defined above.

$v$  is the residual degrees of freedom and is defined as the number of response values  $n$  minus the number of fitted coefficients  $m$  estimated from the response values

A RMSE value closer to 0 indicates a better fit.

### 3.3.5 Curve Fitting Results

It is important to mention that the fits are only performed on the magnitude of the FRFs, as the algorithm does not support complex numbers. Therefore, the 12 accelerance FRFs corresponding to the base of the suspension are fitted using the equation

$$|H(\omega)| = \left| \sum_{i=1}^n \frac{A_i \omega^2}{\omega_{ni}^2 - \omega^2 + 2j\zeta_i \omega_{ni} \omega} \right| \quad (17)$$

And the 3 receptance FRFs corresponding to the head of the suspension are fitted with the following equation

$$|H(\omega)| = \left| \sum_{i=1}^n \frac{A_i}{\omega_{ni}^2 - \omega^2 + 2j\zeta_i\omega_{ni}\omega} \right| \quad (18)$$

As mentioned earlier, there are 13 DOFs therefore 13  $\omega_n$ , 13  $\zeta$ , and 13  $A$  are to be identified for each FRF. There are no restrictions on the damping ratios and gains, and the starting value for the resonance frequencies are set as in [Table 1](#).

Shown below are some sample preliminary curve fitting results, for the accelerance and the receptance FRFs.

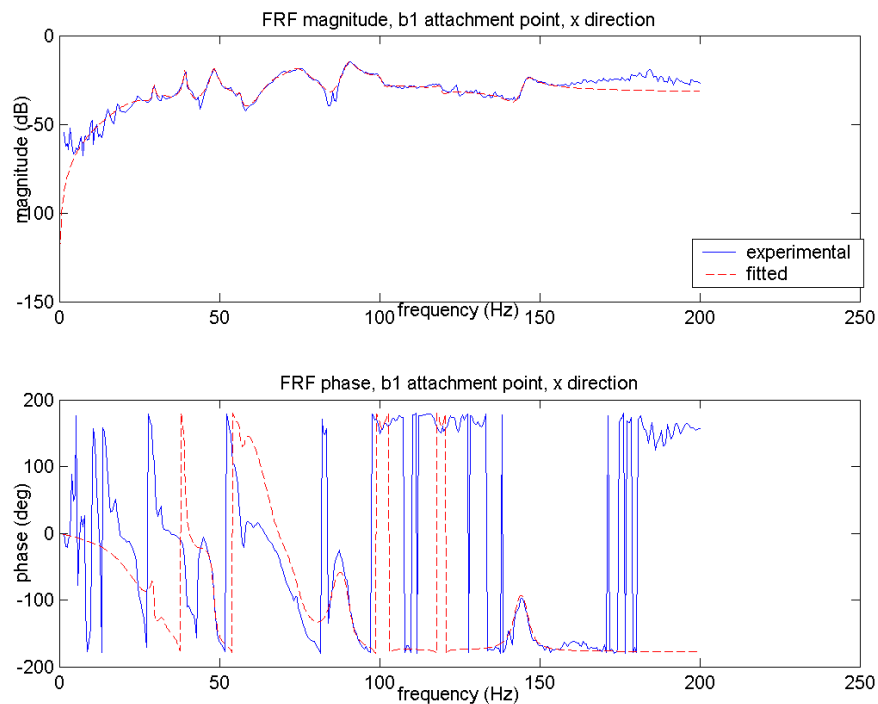


**Figure 17** - Fit performed on the FRF taken at b1, x direction

Mode	Gain	Damping (%)	Freq (Hz)
1	0.01008	3.28	24.13
2	-0.0005087	1.78	29.55
3	0.003155	2.12	32.77
4	-0.00195	0.63	39.38

5	0.003556	1.65	48.12
6	0.01264	1.47	55.87
7	-0.01318	1.52	55.88
8	-0.005359	3.14	65.62
9	0.009772	4.14	74.85
10	0.005829	1.74	90.38
11	-0.0009402	1.49	100.4
12	-0.0002185	0.67	119.3
13	0.001319	1.27	146.0
R-Square		0.9831	
RMSE		0.004628	

**Table 2 - b1-x fit results and statistics**

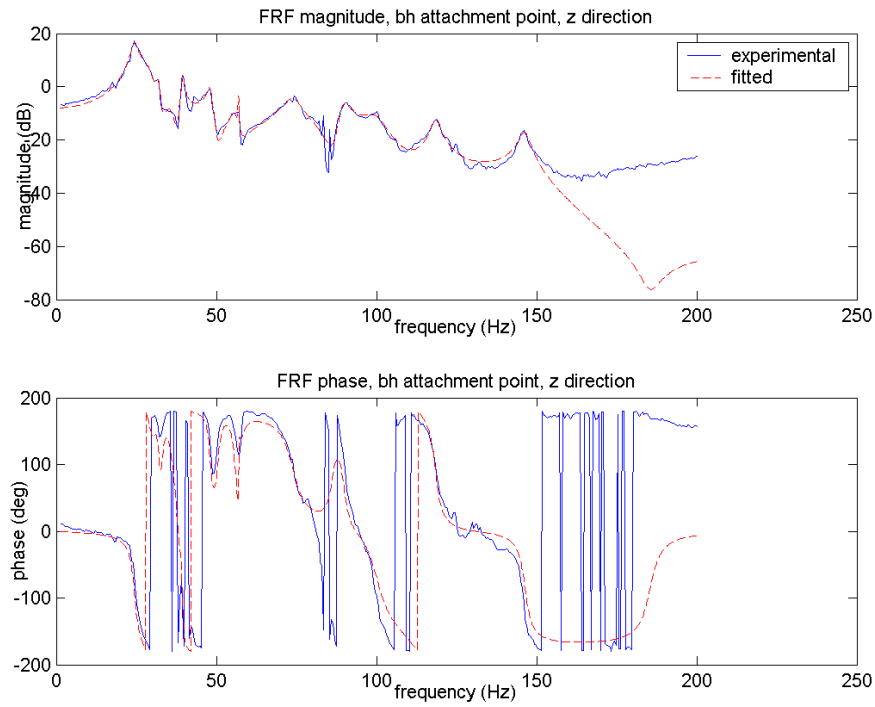


**Figure 88 - Fit performed on the FRF taken at bh, z direction**

Mode	Gain	Damping (%)	Freq (Hz)
1	385	4.69	24.46
2	-113.6	2.34	29.51
3	-35.86	1.84	31.99
4	51.22	0.97	39.4
5	-65.41	1.62	48.03
6	-34.28	1.88	55.72
7	6.873	1.11	56.89
8	-34.96	3.30	64.08
9	-270.5	4.13	73.94
10	-115.2	1.55	89.71
11	200.9	2.56	100.2
12	-82.58	1.18	118.5
13	65.07	1.10	146.4
R-Square		0.9894	
RMSE		0.1016	

**Table 3 - bh-z fit results and statistics**

Since all the fits are performed independently, the damping ratios and the resonance frequencies differ slightly from one fit to the other. They should in theory be identical for all FRFs. Therefore, a common value for each vibration mode is identified that best represents the structure under test. For each DOF, the resonance frequency and damping ratio values from the FRFs where this mode is well defined are averaged in order to yield the definitive nominal parameters that will be used to construct the model. These values are shown in [Table 4](#).

Mode	Frequency (Hz)	Damping (%)
1	24.26	4.41
2	30.00	1.46
3	32.26	1.68
4	39.49	1.68

5	48.44	2.37
6	54.31	1.49
7	56.56	1.16
8	63.49	2.67
9	74.89	3.20
10	90.14	1.60
11	100.275	1.91
12	118.44	0.83
13	145.9	1.27

**Table 4 - modes of vibration of the ¼ car suspension**

Once the vibration modes parameters are identified, a second iteration of the curve-fitting algorithm is necessary to find the gain values corresponding to these new modal parameters.

Throughout this thesis, the output from sensors located at the 1<sup>st</sup> attachment point of the base of the suspension in the x direction, and the head of the suspension in the z direction, are used to illustrate the statements being made. Furthermore, the y and z sensors output at b1 and the x and y sensors output at bh are also included in a smaller format as they usually exhibit a slightly different behaviour. However, the sensors at b2, b3 and b4 in all 3 axes are very similar to the sensors at b1 and therefore are not shown.

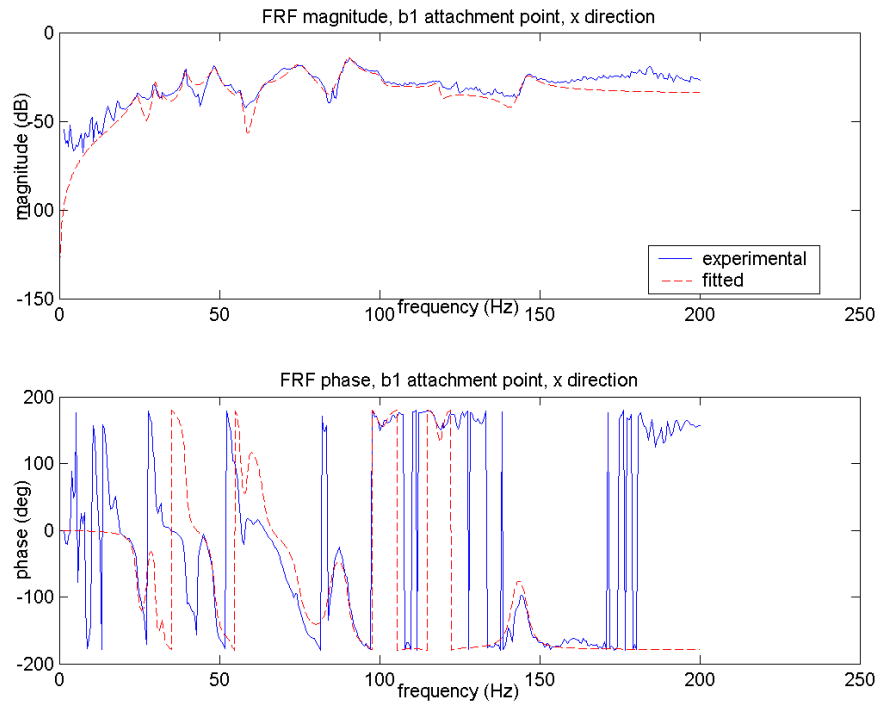


Figure 99 – Second fit performed on the FRF taken at b1, x direction

R-Square	RMSE
0.9345	0.008736

Table 55 - b1-x second fit statistics

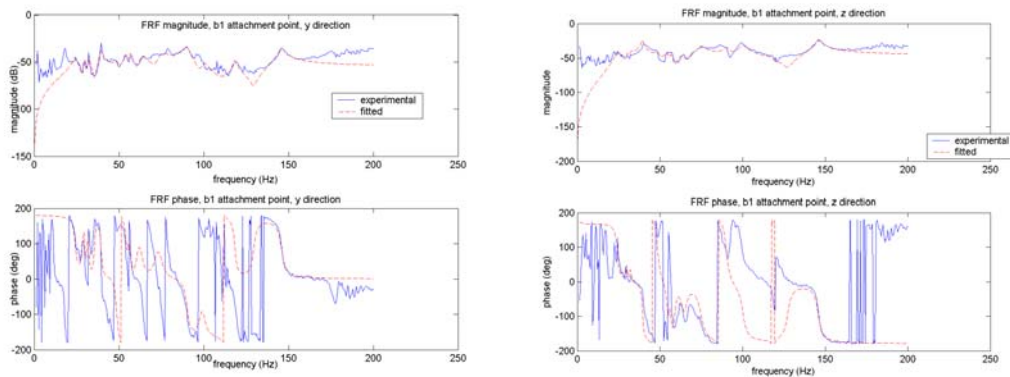
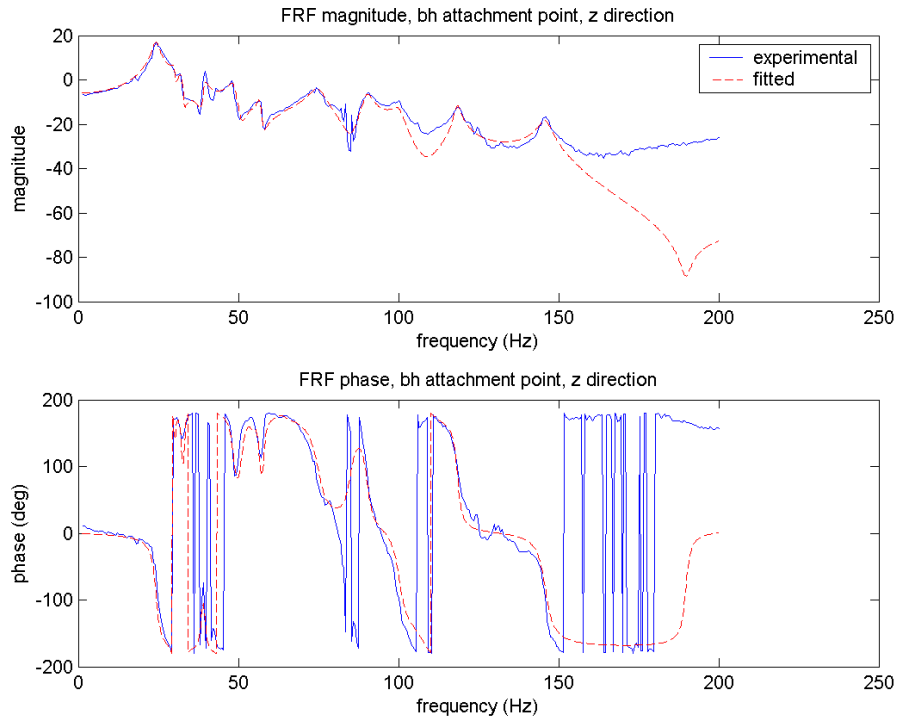


Figure 1040 - Second fit performed on the FRF taken at b1, y (left) and b1, z (right)

R-Square	RMSE
0.7940	0.002021

R-Square	RMSE
0.9096	0.003388

**Table 66 - b1, y (left) and b1, z (right) second fit statistics**



**Figure 1144 - Second fit performed on the FRF taken at bh, z direction**

R-Square	RMSE
0.9885	0.1014

**Table 77 - bh-z second fit statistics**

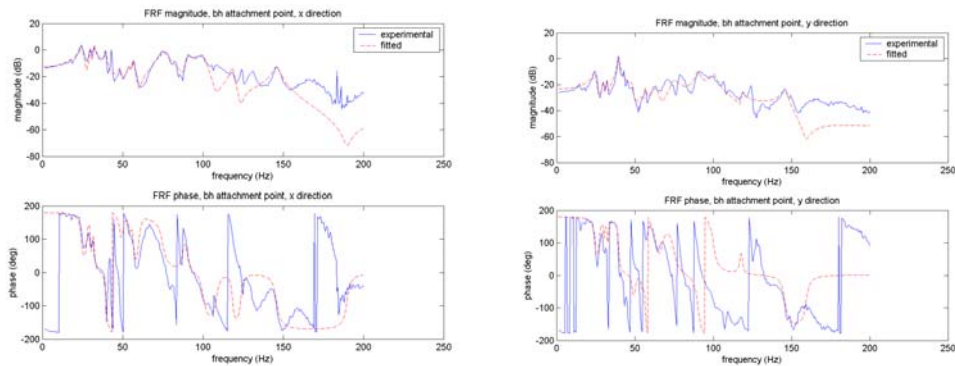


Figure 1242 - Second fit performed on the FRF taken at bh, x (left) and bh, y (right)

R-Square	RMSE	R-Square	RMSE
0.9213	0.07951	0.9274	0.03362

Table 88 - bh-x (left) and b1, y (right) second fit statistics

As can be observed when comparing those fits to the first iteration, they are less accurate and the R-square has decreased slightly. This is understandable since the resonance frequency and damping ratio parameters are fixed and the curve fitting algorithm is only free to adjust the gain for each DOF on the FRFs. Yet, a full description of the structure in terms of its modes of vibrations has now been accomplished and it is now possible to derive a state space model from these modal parameters.

### 3.4 State Space Realization

A state space representation of the ¼ car suspension is more desirable for control analysis and design purposes.

$$\begin{aligned} \dot{x} &= Ax + Bu \\ y &= Cx + Du \end{aligned} \tag{19}$$

Where  $x \in \mathcal{R}^n$  is the state vector,  $\dot{x}$  its derivative and  $u \in \mathcal{R}^m$  is the input vector. A, B, C and D are the state space matrices, and  $y \in \mathcal{R}^m$  is the output vector [[usually p-dimensional, unless the plant is square]]

It is important to note that the state space representation is not unique. There are several state vector and A,B,C,D matrix representations that yield the same input-output relationship. However, which state representation is chosen makes a difference because, while the input-output relationship may not change, some representations have useful physical interpretations while others are more suitable for analysis and design. The modal representation of the system is chosen in this case for the latter reason.

The ¼ car suspension can be represented as a linear flexible structure that fits the following second-order matrix differential equation

$$\begin{aligned} M\ddot{\eta} + D\dot{\eta} + K\eta &= B_o u \\ y &= C_\eta \eta + C_v \dot{\eta} \end{aligned} \quad (20)$$

Where  $\eta$  is the displacement vector,  $\dot{\eta}$  its first derivative,  $u$  is the input value,  $y$  is the output vector,  $M$  is the mass matrix,  $D$  is the damping matrix (not the same matrix  $D$  as defined in equation (19)-(19)),  $K$  is the stiffness matrix,  $B_o$  is the input matrix,  $C_\eta$  is the output displacement matrix and  $C_v$  is the output velocity matrix

In order to obtain a state representation, equation (20)-(20) is rewritten (the mass matrix is assumed nonsingular)

$$\begin{aligned} \ddot{\eta} + M^{-1}D\dot{\eta} + M^{-1}K\eta &= M^{-1}B_o u \\ y &= C_\eta \eta + C_v \dot{\eta} \end{aligned} \quad (21)$$

We can define the state vector as

$$x = \begin{bmatrix} \eta \\ \dot{\eta} \end{bmatrix} \quad (22)$$

Where the first component is the modal displacement and the second component is the modal velocity.

From these equations it is possible to derive the state space representation

$$A = \begin{bmatrix} 0 & I \\ -M^{-1}K & -M^{-1}D \end{bmatrix}, \quad B = \begin{bmatrix} 0 \\ M^{-1}B_o \end{bmatrix}, \quad C = [C_\eta \quad C_v] \quad (23)$$

The dimension of the state space model is twice the number of DOFs since each DOF has two states.

These equations give a state space representation of the system but it is not possible to directly relate them to the modal parameters. A similarity transformation is therefore needed [11, 12] which will yield the following equation based on equation (21)-(21) for the  $i^{\text{th}}$  degree of freedom [[the state changes after application of the similarity transformation: better to use a different notation. I suggest to keep eta for this new state and using, say, q for the state in (20)-(21)]]

$$\ddot{\eta}_i + 2\zeta_i \omega_{ri} \dot{\eta}_i + \omega_{ri}^2 \eta_i = f_i \quad (24)$$

Where  $f_i$  is the modal load. [[you should stick to wni notation instead of wri for natural undamped frequency]]

It is now a simple matter to transform the second-order differential equation (24) into a set of first-order differential equations

$$\begin{bmatrix} \dot{\eta}_i \\ \ddot{\eta}_i \end{bmatrix} = \begin{bmatrix} 0 & 1 \\ -\omega_{ri}^2 & -2\zeta_i \omega_{ri} \end{bmatrix} \begin{bmatrix} \eta_i \\ \dot{\eta}_i \end{bmatrix} + \begin{bmatrix} 0 \\ b_i \end{bmatrix} u \quad (25)$$

Note that the modal input  $f_i$  is replaced by the control input  $b_i$  [[Here the bi's are row vectors if the plant is multi-input: mention]] in equation (25); this equation forms the basis of the modal state space representation. Generalizing for  $n$  degrees of freedom :

$$\begin{bmatrix} \dot{\eta}_1 \\ \ddot{\eta}_1 \\ \vdots \\ \dot{\eta}_n \\ \ddot{\eta}_n \end{bmatrix} = \begin{bmatrix} \begin{bmatrix} 0 & 1 \\ -\omega_{r1}^2 & -2\zeta_1 \omega_{r1} \end{bmatrix} & & & 0 \\ & \ddots & & \\ & & \begin{bmatrix} 0 & 1 \\ -\omega_{rn}^2 & -2\zeta_n \omega_{rn} \end{bmatrix} & \\ 0 & & & \end{bmatrix} \begin{bmatrix} \eta_1 \\ \dot{\eta}_1 \\ \vdots \\ \eta_n \\ \dot{\eta}_n \end{bmatrix} + \begin{bmatrix} 0 \\ b_1 \\ \vdots \\ 0 \\ b_n \end{bmatrix} u \quad (26)$$

It is now possible to directly relate the modal parameters to the A and B matrices of the state space representation.

$$\dot{x} = Ax + Bu \quad (27)$$

Similarly, the C matrix now takes the form

$$C = \begin{bmatrix} c_{11} & 0 & \dots & c_{1n} & 0 \\ \vdots & \vdots & \ddots & \vdots & \vdots \\ c_{m1} & 0 & \dots & c_{mn} & 0 \end{bmatrix} \quad (28)$$

With  $n$  DOFs and  $m$  outputs [[again, p outputs unless the plant is Square]]

The next step in obtaining a state space representation is finding the coefficients [[vectors?]]  $b_1 \dots b_n$  and  $c_1 \dots c_n$ . Let us define the residue matrix R as the matrix containing the gains for all modes from all FRFs.  $R_i$  contains the  $i^{\text{th}}$  mode gains from all

FRFs. It is possible to achieve a minimal state space system by computing, for each mode, the singular value decomposition of the residue matrix  $R_i$ .

The Singular Value Decomposition (SVD) of an  $m \times n$  matrix is given by

$$R_i = U\Sigma V^T \quad (29)$$

Where  $U$  and  $V$  are orthogonal and  $\Sigma$  is an  $m \times n$  diagonal matrix with real diagonal elements,  $\sigma_i$ , such that  $\sigma_1 \geq \sigma_2 \geq \dots \sigma_{\min(m,n)} \geq 0$ . The  $\sigma_i$  are the singular values of  $R_i$  and the first  $\min(m,n)$  columns of  $U$  and  $V$  are the left and right singular vectors of  $R_i$ .

Equation (29) can be further modified to obtain the SVD of the residue matrix,

$$R_i = U\Sigma V^T = \{c\varphi_i\} \{\varphi_i^T b\}^T \quad (30)$$

Where  $\varphi_i$  is the mode shape matrix. [\[shouldn't it be bi and ci, both row vectors??\]](#)

Equation (18), the receptance transfer function, can be rewritten using the result of equation (30)

$$H(s) = \sum_{i=1}^n \frac{\{c\varphi_i\} \{\varphi_i^T b\}^T}{s^2 + 2\zeta_i \omega_{ni} s + \omega_{ni}^2} \quad (31)$$

Once the input and output shape matrices are obtained, it is possible to derive the B and C matrices coefficients. Note that in this equation, all b and c coefficients may be non-zero. This is because the formula is generalized for models that may not have modal damping [13].

$$\begin{bmatrix} c_{1i} \\ c_{2i} \end{bmatrix} = \frac{1}{\omega_{ri} \sqrt{(1-\zeta_i^2)}} \begin{bmatrix} \omega_{ri} \sqrt{(1-\zeta_i^2)} & \zeta_i \omega_{ri} \\ 0 & 1 \end{bmatrix} \begin{bmatrix} \text{Re}(c\varphi_i) \\ \text{Im}(c\varphi_i) \end{bmatrix} \quad (32)$$

$$\begin{bmatrix} b_{j1} & b_{j2} \end{bmatrix} = 2 \begin{bmatrix} \text{Re}(\varphi_i^T b) & \text{Im}(\varphi_i^T b) \end{bmatrix} \begin{bmatrix} 1 & 0 \\ \zeta_i \omega_{ri} & -\omega_{ri} \sqrt{(1-\zeta_i^2)} \end{bmatrix} \quad (33)$$

The state space model thus created outputs displacement for the suspension base sensors and force for the suspension head sensors.

The resulting realization, representing the 13 identified DOFs of the suspension, yields a 26<sup>th</sup> order model with a 26x26 A matrix, 26x1 B matrix, 15x26 C matrix and a null D matrix.

[[I think this section still needs to be cleaned up. It is not clear if the b's and c's are vectors or scalars. Your plant is SIMO, so you could mention this fact and either do the general MIMO derivation with specialization to SIMO at the end, or start with SIMO]]

### 3.5 Model Discretization

A full state space model describing the dynamics of a ¼ car suspension is now available on which to start the design of a controller. However, the model is in continuous time and thus cannot be used in practice, since all the apparatus works in discrete time. It is therefore desirable to convert immediately the model to discrete-time. The conversion is done in Matlab using the Zero-Order Hold method. The following diagram shows the discretization of a continuous LTI system  $H(s)$  into a system  $H_d(z)$ .

[[use MathType]]

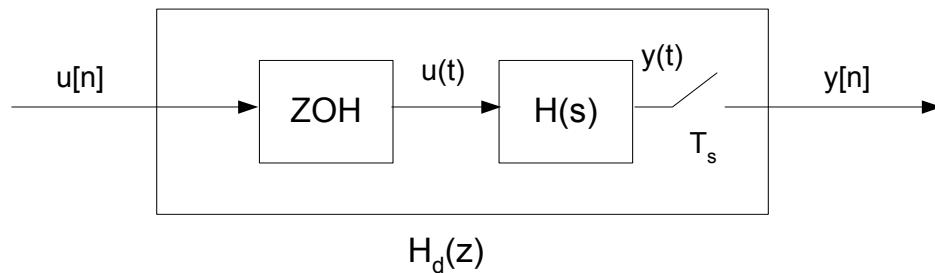


**Figure 1343 – Zero-order hold discretization method**

The ZOH block generates a continuous-time input signal  $u(t)$  by holding each sample value  $u[n]$  constant over one sample period. The signal  $u(t)$  is then fed to the continuous-time system  $H(s)$  and the resulting output  $y(t)$  is sampled every  $T_s$  seconds to produce  $y[n]$ .

[14] The discretization process creates a new set of discrete matrices F, G, H that correspond to the continuous-time set of matrices A, B, C.

$$\begin{aligned}x[n+1] &= Fx[n] + Gu[n] \\y[n] &= Hx[n]\end{aligned}\tag{34}$$

The discretization process requires the computation of the state transition matrix  $\Phi(t)$ , which is computed using the matrix exponential  $e^{At}$  time-shifted to  $t_0$ .

$$\Phi(t-t_0) = e^{A(t-t_0)}\tag{35}$$

Combining the zero-state and zero-input state responses yields the state response of the continuous-time state-space system

$$x(t) = e^{A(t-t_0)}x(t_0) + \int_{t_0}^t e^{A(t-\tau)}Bu(\tau)d\tau\tag{36}$$

Considering that the input  $u(t)$  is held constant during every sampling period, we can take  $t_0 = kT$  and  $t = (k+1)T$  [\[\[use MathType\]\]](#) where  $T$  is the sampling period. Equation [\(36\)](#)~~(36)~~ can then be rewritten and solved as :

$$x((k+1)T) = e^{AT}x(kT) + A^{-1}[e^{AT} - I_n]Bu(kT)\tag{37}$$

A discrete-time system is defined as  $x[n] = x(nT)$ . Comparing equations [\(34\)](#)~~(34)~~ and [\(37\)](#)~~(37)~~, it is therefore possible to compute the discrete-time F matrix

$$F = e^{AT} = L^{-1}(sI-A)^{-1}\tag{38}$$

Where  $L^{-1}$  denotes the inverse Laplace transform.

Also from equation [\(37\)](#)~~(37)~~, the discrete-time input gains matrix  $G$  is defined as

$$G = A^{-1}[e^{AT} - I_n]B\tag{39}$$

The output equation remains unchanged in discrete-time, so the  $H$  matrix is equal to the continuous-time output gains matrix  $C$  :

$$H = C\tag{40}$$

Throughout the discretization process, the ~~sample~~[e-timeing period](#) used is 0.001 second, corresponding to a sampling frequency of 1000Hz, so as to be consistent with the sampling frequency used during the experimental data acquisition on the test bench.

As can be seen in the following sample bode plot created from the b1 attachment point, x direction output, no data is lost during the discretization process. The discrete model does not approximate the continuous time model correctly near the nyquist frequency (500 Hz), but that is well outside the frequency range of interest (20-160 Hz)

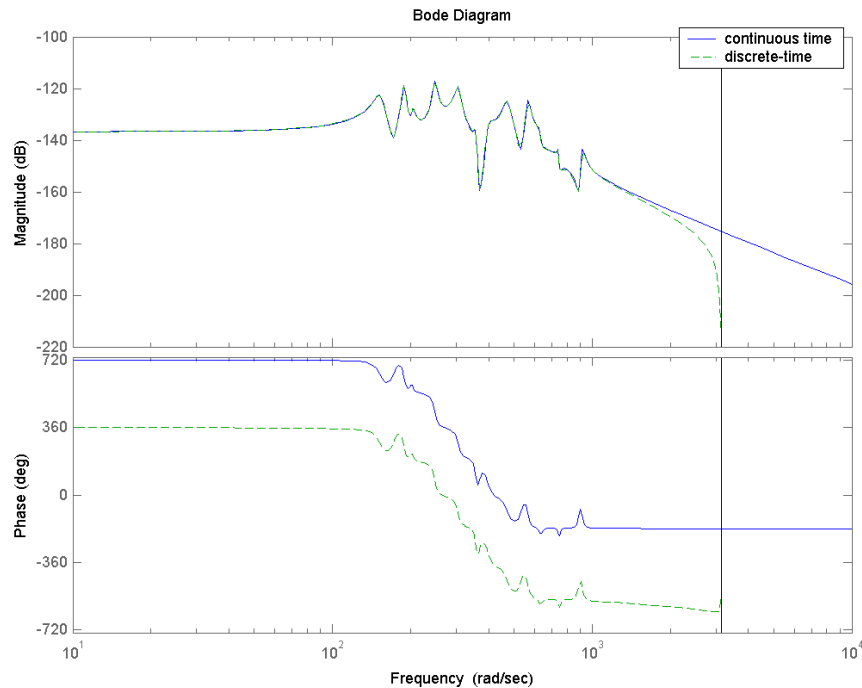


**Figure 1414 – Comparison of continuous-time and discrete-time bode plots**

Since the discrete-time state-space model of the  $\frac{1}{4}$  car suspension is used to design the controllers, simulate the controlled system and evaluate the controllers' performance, its stability must be assessed. A discrete-time system is considered stable if all its poles are inside the unit circle. Since the actual system is stable (it would actually be funny to see an unstable car suspension), a correct model of the suspension must therefore be stable as well. As can be seen in [Figure 15](#), all poles are inside the unit circle therefore the model is stable.

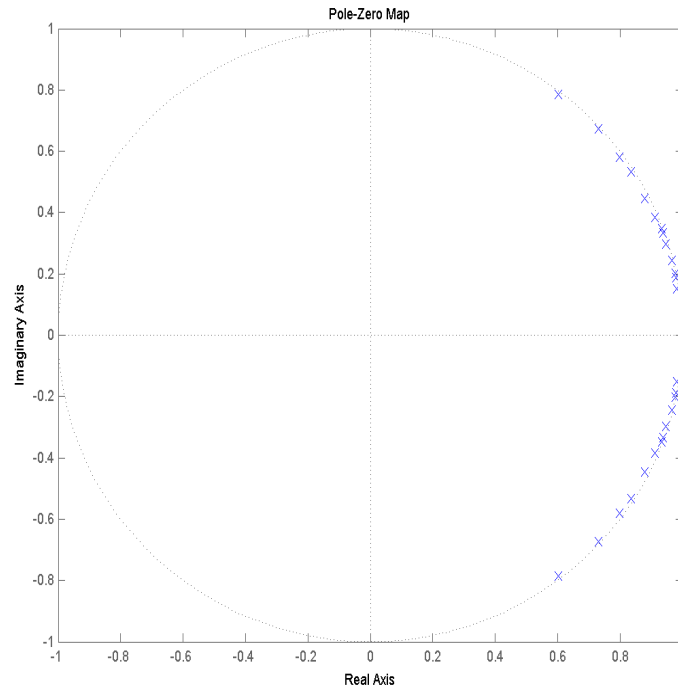
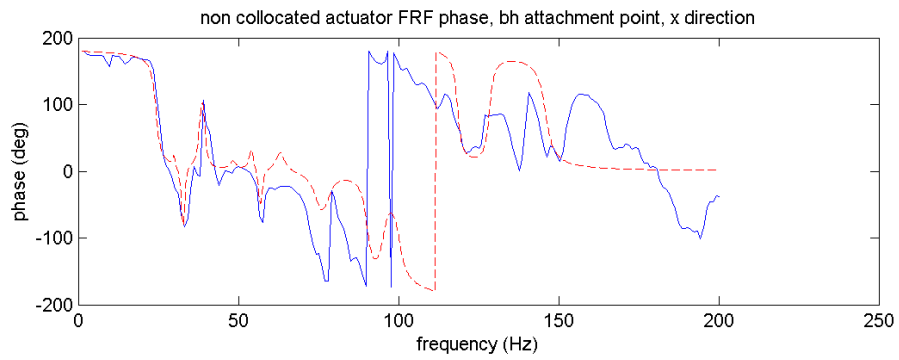
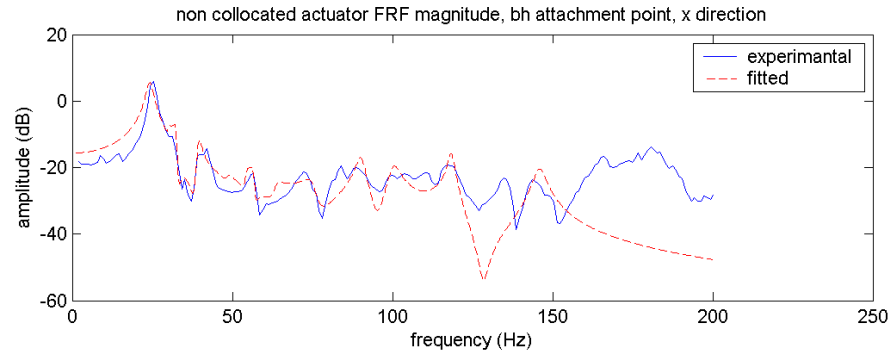


Figure 1545 – Pole-zero plot of the discrete-time state space model

### 3.6 Non-Collocated Actuator

The model derived in the previous sections assumes that the actuator is collocated with the disturbance at the axle of the wheel. However, for practical purposes, the actuator cannot be installed at that location on a vehicle. It is therefore necessary to obtain a second set of FRFs with the actuator located at one of the attachment points of the suspension to the car frame. The following FRFs are obtained by positioning the shaker underneath the lower attachment points on the experimental test bench, acting in the  $z$  direction.



**Figure 1646** – bh-x receptance FRF, actuator non-located

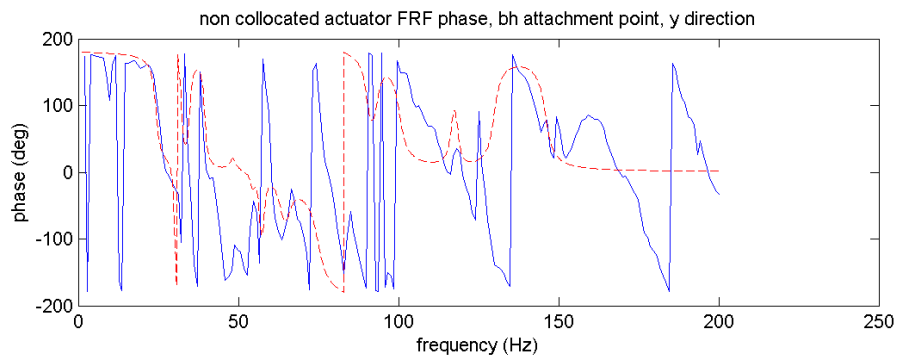
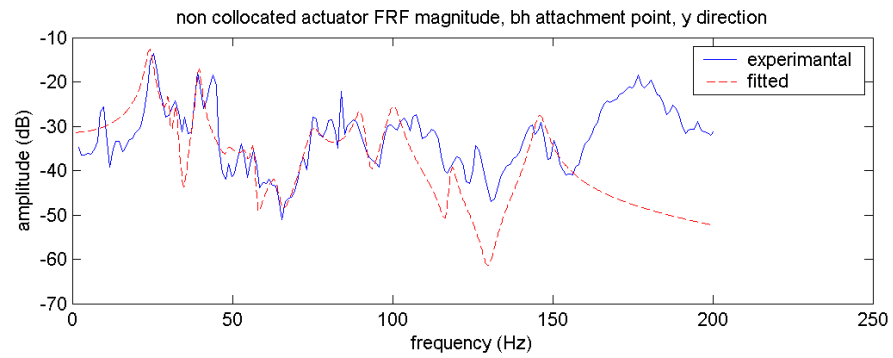


**Figure 1747** – bh-y receptance FRF, actuator non-located

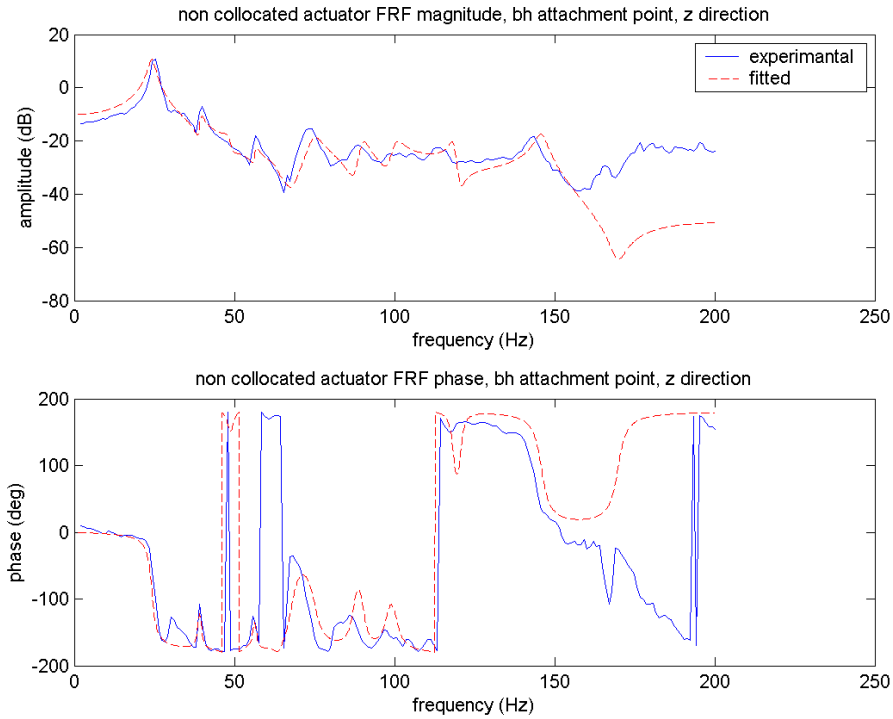


**Figure 1848 – bh-z receptance FRF, actuator non-collocated**

Since the undamped natural frequencies and damping ratios are characteristics of a structure, they are not influenced by the excitation location. However, the amplitude of the response as measured at the sensor locations varies with the actuator location. Therefore, the FRFs need to be curve-fitted using the method described previously to identify the new set of gains. A second B matrix is added to the state-space system to account for the different actuator location.

$$\begin{aligned} \dot{x} &= Ax + B_a u_a + B_d u_d \\ y &= Cx + Du \end{aligned} \quad (41)$$

Where  $u_a$  is the actuator input with the corresponding input gains matrix  $B_a$ , while  $u_d$  is the actuator input with the corresponding input gains matrix  $B_d$ .  $B_d$  is as previously computed, and the A, C and D matrices remain as before since the structure has not changed. The whole system is also discretized as previously described.

### 3.7 Model Limitations

The complete discrete-time state-space model, as accurate as it is, still suffers from several limitations. Since it is based on experimental data acquisition, there is a certain amount of uncertainty on the data due to noise, numerical accuracy or the physical limitations of the sensors. This uncertainty translates into FRFs that may contain some error, as is demonstrated by the coherence function. The next step, the curve-fitting process, also introduces uncertainty on the model, as it is impossible to exactly fit the FRF data. Due to the necessity of having a finite and manageable number of DOFs, certain modes have to be ignored, as well as the modes outside the frequency range of interest that may have an effect on the response in the frequency range of interest. This can lead to a certain additional uncertainty on the modal parameters as well.

Finally, the structure is assumed to be LTI. However, certain operating conditions may cause the structure to be time varying (such as temperature variations, wear of the mechanical components). The suspension also contains such non-linearities as hard bounds or elasticity. Because of the LTI assumption, these time-varying and non-linear components are not incorporated into the model.

### 3.8 System simulation

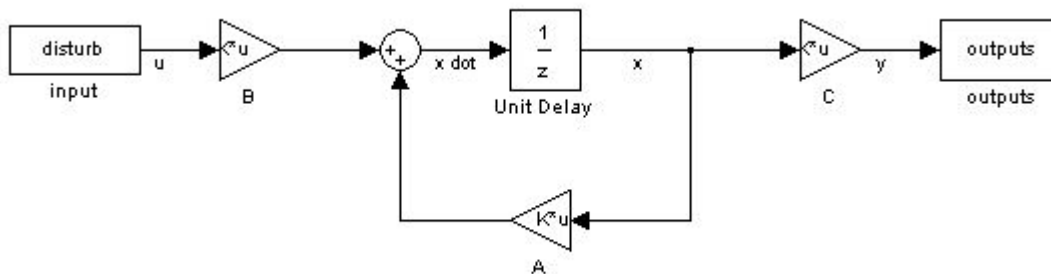
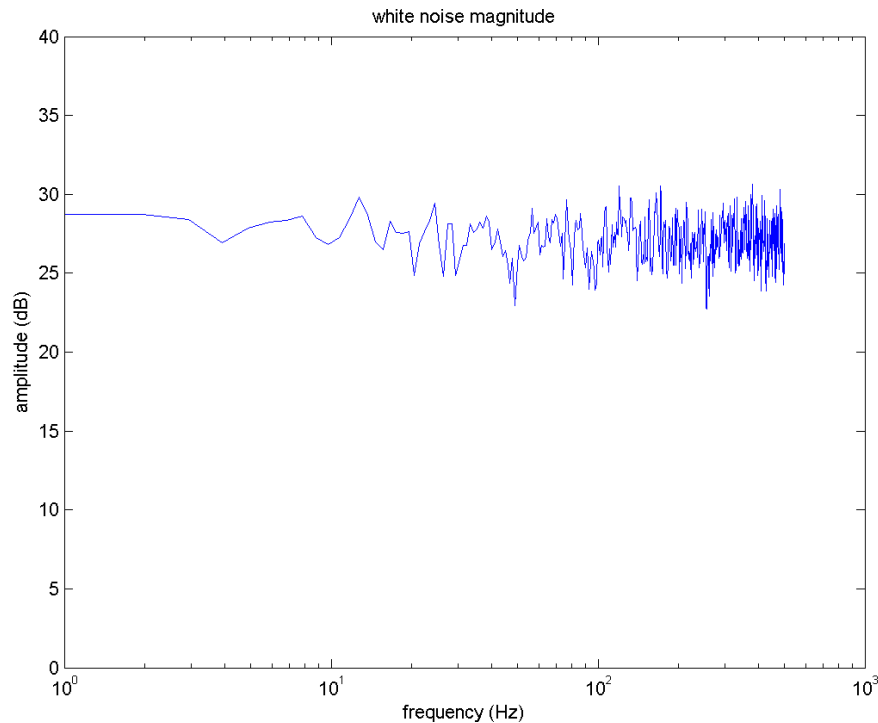


Figure 1949 – Simulink simulation of discrete model

The completed model is simulated in Simulink. The disturbance is simulated as a white noise of amplitude similar to that used during the experimental data acquisition and

band-limited at 500 Hz. The white-noise generator included in Simulink however does not generate true white noise, as its magnitude is not uniform over the whole frequency spectrum. Therefore, the white noise is generated in Matlab using the random number generator. ~~Figure 20~~ **Figure 20** shows the FFT of the white noise used.



**Figure 2020 – FFT of white noise disturbance**

The input gains matrix  $B$  used in this case is  $B_d$ , representing an actuator located at the wheel axle. The simulation lasts for 20 seconds, enough to have a good coherence value. The output is recorded and then compared to the fitted data. The same function is used to create the  $H$ ,  $H_1$ ,  $H_2$  and coherence values as with the experimental data. A 2048 points FFT seems to yield the best results, as a higher number of points degrade the high frequency coherence and a smaller number of points degrade the low frequency performance. ~~Figure 21~~ **Figure 21** compares the simulated FRF to the fitted data for the b1 attachment point, x direction sensor, validating the state-space model and the method of simulation.

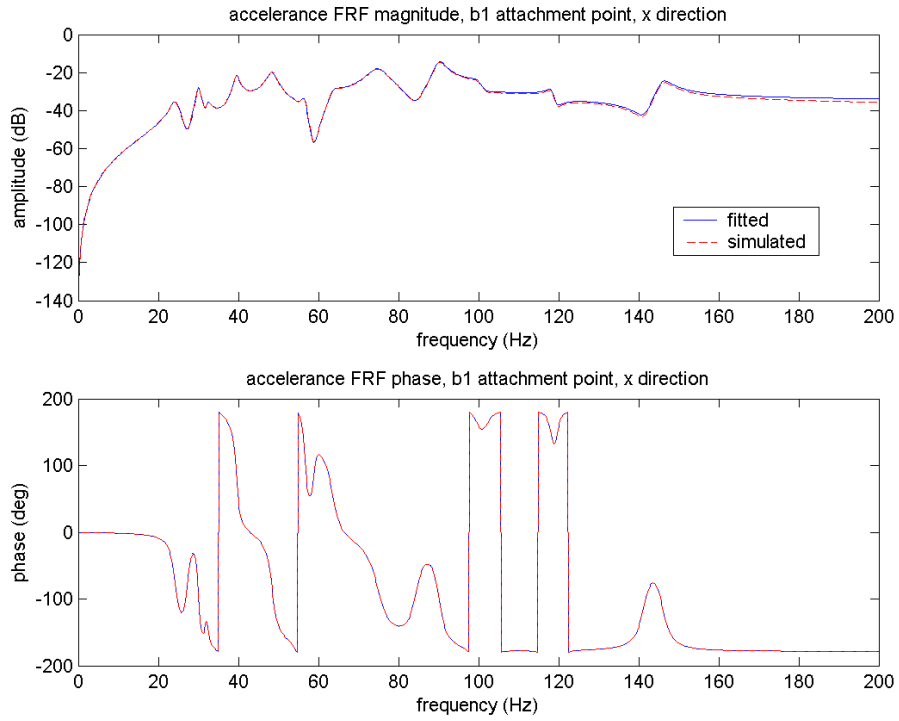
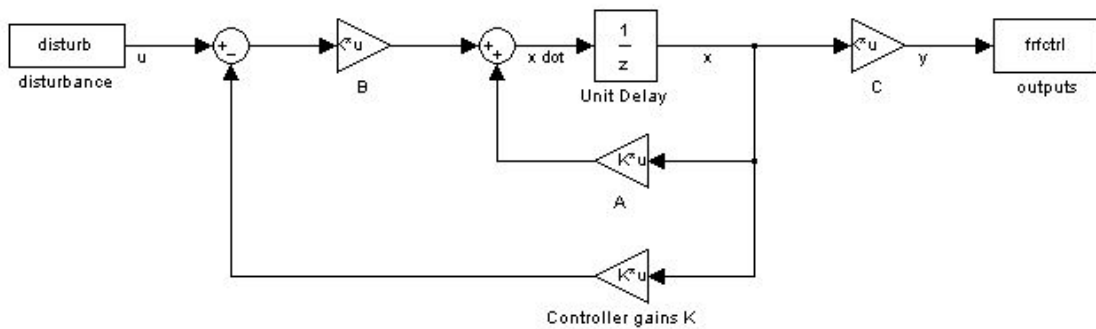


Figure 2124 – FRFs taken from the b1 attachment point, x direction output

# 4 Controller Design

## 4.1 State-Feedback Regulator design

The aim of the controller is to keep the vibrations as low as possible, ideally to 0. Therefore, a state feedback regulator is designed with a desired value of 0. The feedback signal goes through the controller, which outputs a control signal to offset the disturbance introduced to simulate road-induced vibrations. [Figure 22](#) shows the regulator implementation. The actuator is assumed to be collocated with the disturbance in this case.



**Figure 2222** – Regulator implementation with a collocated actuator

In the case where the actuator is not collocated with the disturbance, the Simulink diagram must be modified to reflect this case, as the input gains ( $B$ ) matrix is different for the actuator and for the disturbance.

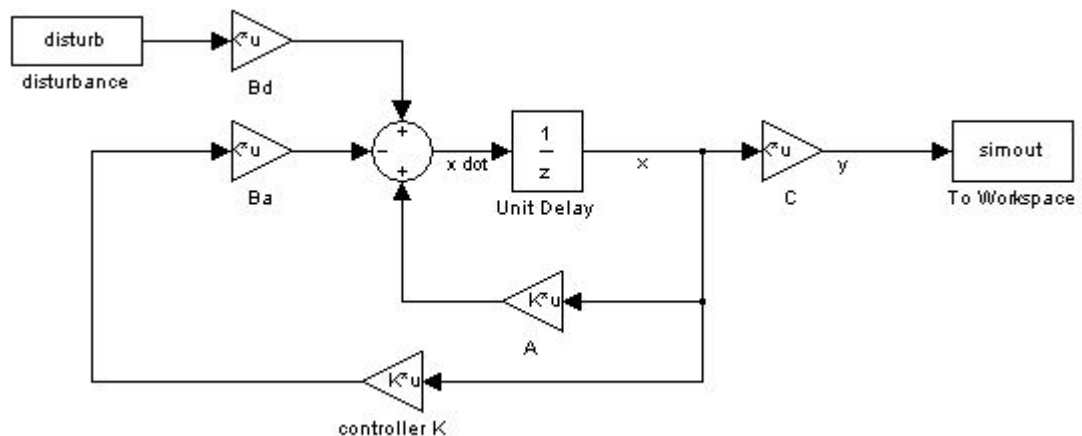


### Figure 2323 - Regulator implementation with a non-collocated actuator

To simulate a real working environment, noise is introduced on the outputs. The magnitude of the noise is about 10 % of the sensor signal magnitude. Figure 24 shows the comparison of the output signal and noise magnitude on the x-direction sensor located at B1. The left graph shows the sensor signal magnitude, while the right graph shows the sensor noise magnitude.

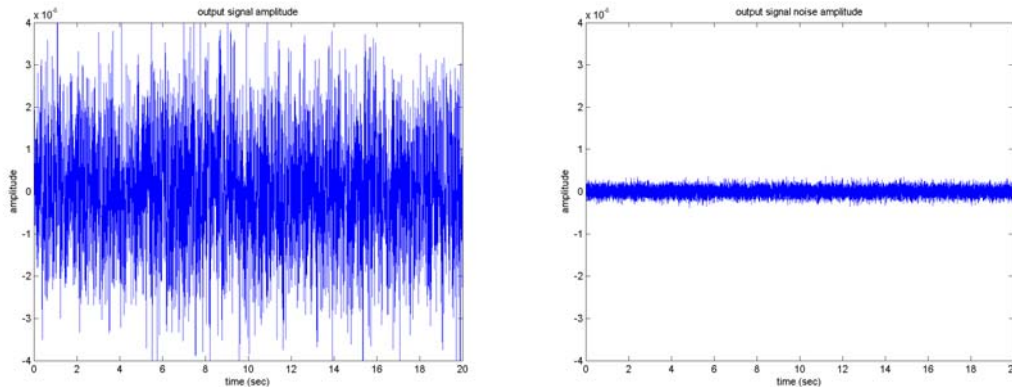


Figure 2424 – Output Signal and noise magnitude comparison for the b1, x direction sensor

The controller requires the value of all the system states to compute the control signal. However, since only the outputs from the 15 sensors are available, an observer is necessary to reconstruct the states. The next section describes the design of a Kalman filter to act as a state observer.

## 4.2 Kalman Filter

### 4.2.1 Design

The Kalman filter is a state observer used to reconstruct a system's states when they are not directly measurable. It uses a model, the inputs and the outputs of the real system to estimate the values of the states. However, the filter may not have access to the full input to the system. In the present case, the actuator input is known while the disturbance input is unknown. Therefore, the resulting output as computed by the observer will differ with the real system's output. This difference, multiplied with a set of gains called the Kalman gains, is added to the estimated state to correct for such

unknowns and adjust the estimates. The Kalman gains are updated each iteration and eventually converge to a steady-state value. Covariance matrices are also incorporated into the filter to account for process and sensor noise.

The Kalman filter takes as input the state estimate at time  $k$  as well as the input, and computes the state estimate at time  $k + 1$ , given  $x(k)$

$$\hat{x}(k + 1 | k) = F(k)\hat{x}(k | k) + G(k)u(k) \quad (42)$$

[[best to use "Math" style in MathType]]The next step is to compute the measurement prediction

$$\hat{z}(k + 1 | k) = H(k + 1)\hat{x}(k + 1 | k) \quad (43)$$

The measurement prediction is subtracted from the real measured outputs to yield the measurement residual

$$v(k + 1) = z(k + 1) - \hat{z}(k + 1 | k) \quad (44)$$

The state estimate is then updated using the measurement residual and the Kalman gains  $W(k+1)$

$$\hat{x}(k + 1 | k + 1) = \hat{x}(k + 1 | k) + W(k + 1)v(k + 1) \quad (45)$$

The Kalman gain matrix is  $2n \times p$ , where  $n$  is the number of DOFs and  $p$  the number of output sensors. The individual gains are computed using state and noise covariance matrices. The state covariance at time  $k$  is written as  $P(k | k)$  and is used to compute the state prediction covariance  $P(k + 1 | k)$  and the innovation covariance  $S(k + 1)$

$$P(k + 1 | k) = F(k)P(k | k)F(k)' + Q(k) \quad (46)$$

$$S(k + 1) = H(k + 1)P(k + 1 | k)H(k + 1)' + R(k) \quad (47)$$

Where  $Q(k)$  and  $R(k)$  are respectively the process noise and the output noise covariance matrices

The filter gains may now be computed

$$W(k+1) = P(k+1|k)H(k+1)'S(k+1)^{-1} \quad (48)$$

And the state covariance matrix is updated.

$$P(k+1|k+1) = P(k+1|k) - W(k+1)S(k+1)W(k+1)' \quad (49)$$

Figure 25 shows how the above equations are implemented in Simulink

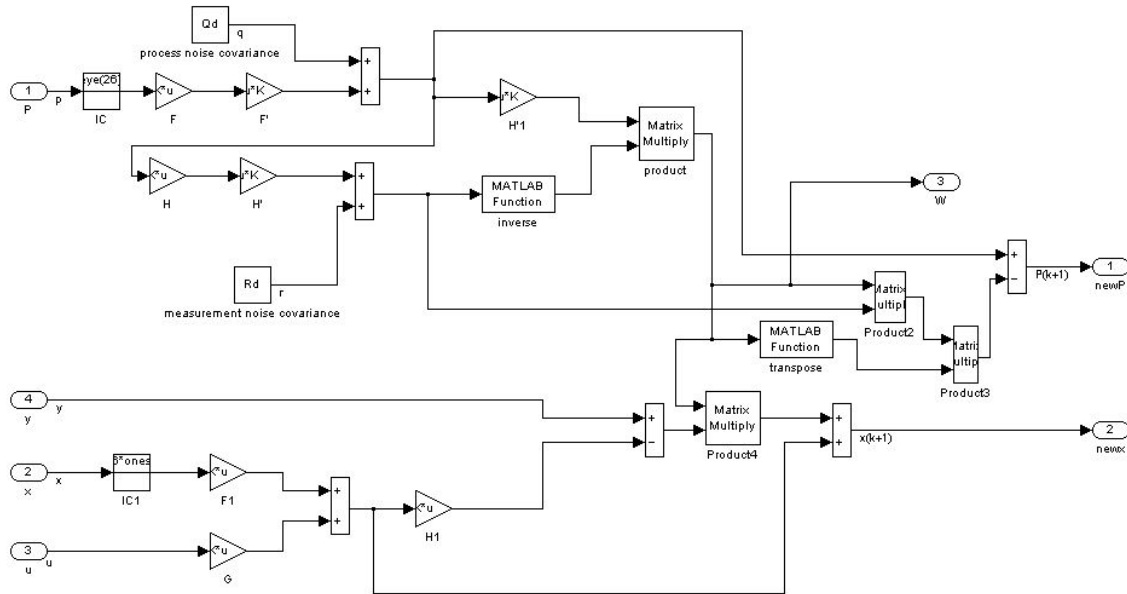
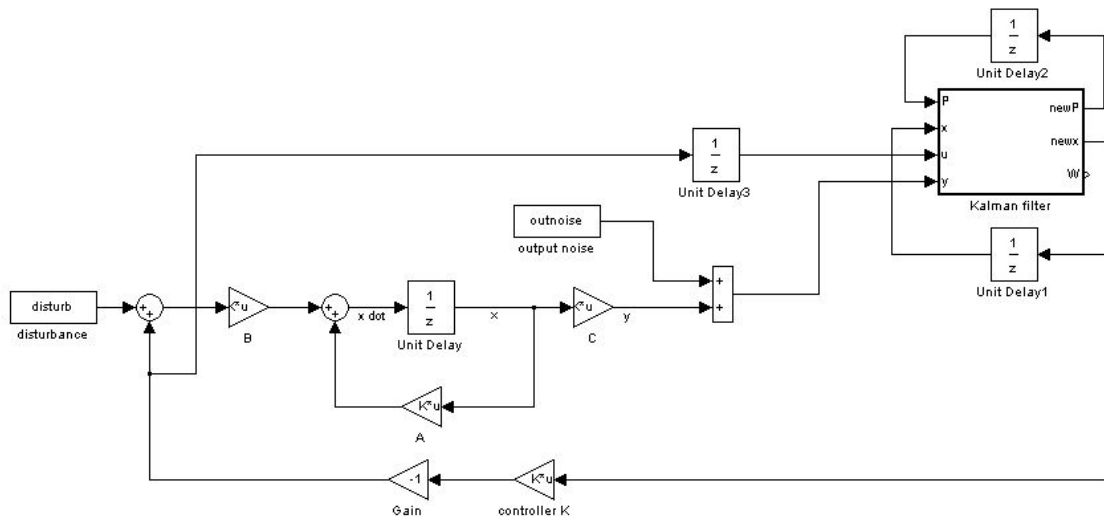


Figure 25 – Kalman Filter implementation

Figure 26 shows the closed-loop system with the Kalman filter.



## Figure ~~26~~26 – Regulator including Kalman filter

The process and output noise covariance matrices are diagonal matrices with respectively  $2n$  and  $m$  elements on the diagonal, where  $n$  is the number of DOFs and  $m$  is the number of output sensors. The elements on the diagonal of the output covariance matrix are the square of the noise amplitude value added to their respective output. For example, if a white noise of maximum amplitude  $1 \times 10^{-3}$  is added to the third output, the third element of the output noise covariance matrix is  $1 \times 10^{-6}$ .

### 4.2.2 Results

When simulating the complete system with the Kalman filter included, it is necessary to provide initial conditions for the state estimates and the state covariance. The resulting filter gains will therefore not be accurate for the first iterations, and will converge towards their final values as the simulation progresses. In the present case, there are 26 states to be constructed from 15 output signals, creating a  $26 \times 15$  Kalman Gains matrix. ~~Figure 27~~Figure-27 shows the values of one of the filter gains to provide an idea of the convergence speed. All gains converge at the same speed.

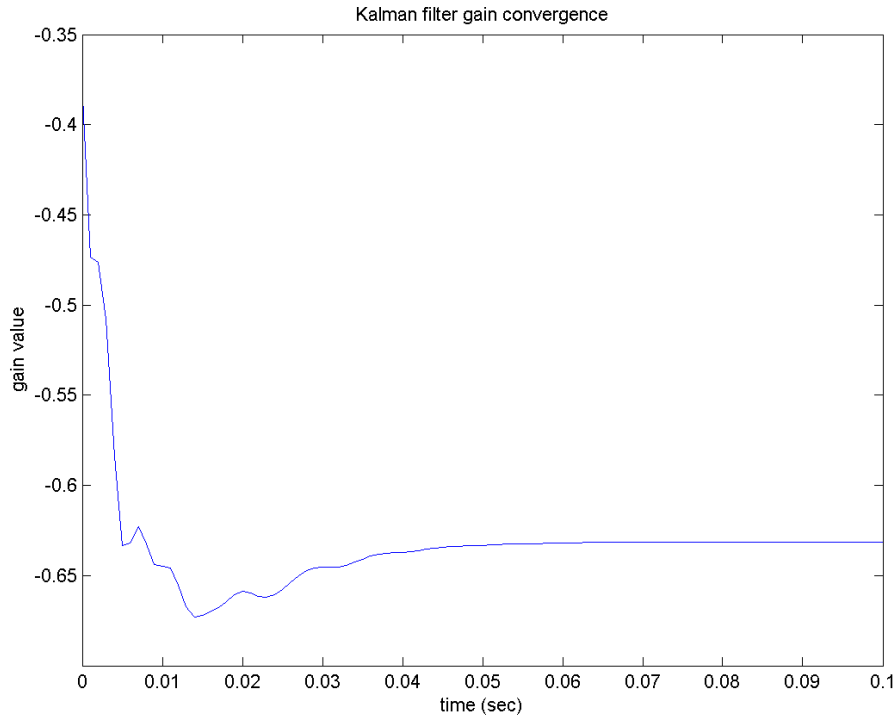


**Figure 2727 – Sample filter gain convergence**

As can be observed, the Kalman gains reach their steady-state value before 0.1 seconds of simulation, and hold this value for the remainder of the simulation. The quality of the reconstruction is shown in the following figures using the first state (1<sup>st</sup> mode displacement) as example.

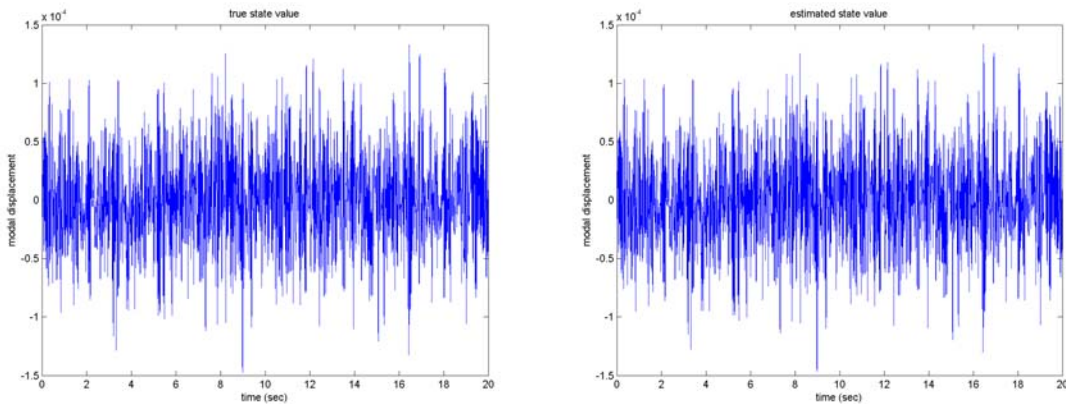


**Figure 2828 – First state true value (left) and estimated value (right)**

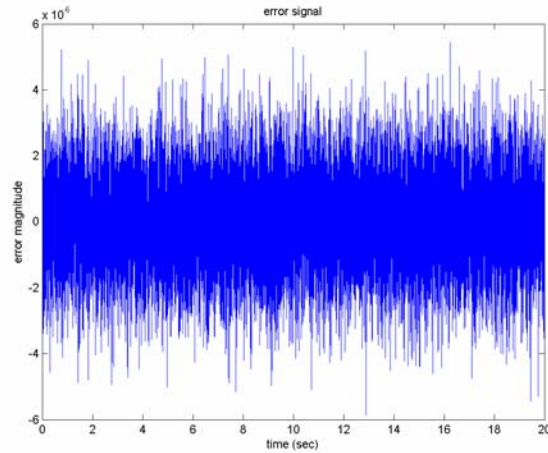


Figure 29 – error on the first state

Figure 28 compares the true value of the first mode displacement to the estimated value throughout the 20 seconds simulation. Figure 29 shows the error on the estimation to be no greater than  $6 \times 10^{-6}$  m, which corresponds to a mean error of 3,84 % of the true state's value.

The Kalman filter, on the other hand, does not reconstruct the modal velocities with as much precision as the modal displacement, as is demonstrated in the following figures for the modal velocity of the first mode (second state).

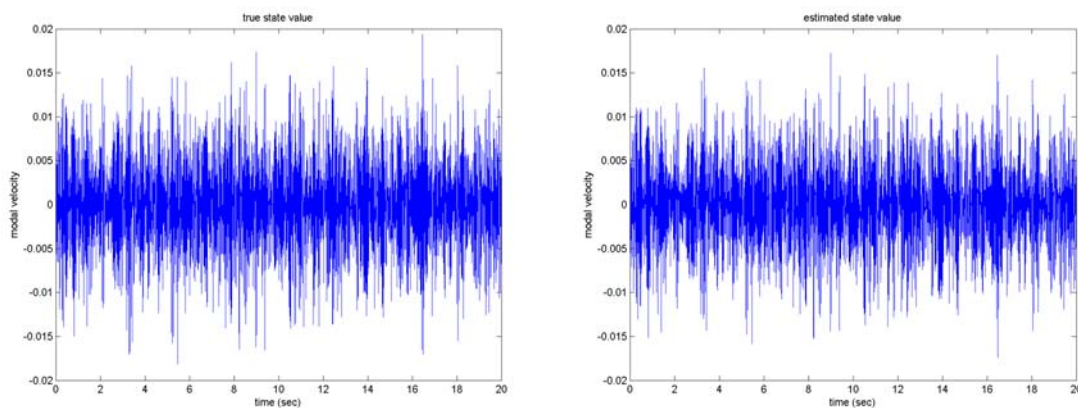
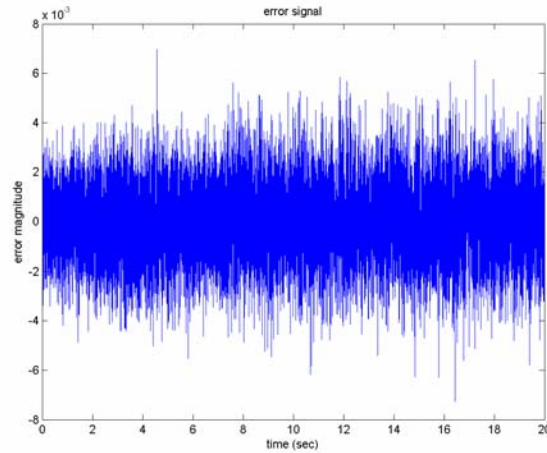


Figure 30 – Second state true value (left) and estimated value (right)



**Figure 3134 – Error on the second state**

The mean magnitude of the modal velocity of the first mode is 0.0038 m/s, with a mean error on the reconstruction of 0.0012 m/s, which corresponds to an error of 31,6 %.

The error on both the estimation of the modal displacements and modal velocities of the remaining 12 modes is of the same order of magnitude as for the first mode. Because of this error, a loss of performance in the attenuation of the resonance peaks is to be expected when the Kalman filter is added to the feedback loop in the simulation.

A major drawback of the Kalman filter is that the matrix inversion during the computation of the filter gains ~~makes it is~~ very computationally intensive, making it ~~very~~ difficult to implement in a real-time environment. A solution to this is to assume that the process and noise covariance matrices are constant. Therefore, the gains computed using Kalman's algorithm, once they have converged to their final value, will not change. It is thus possible to compute the Kalman gains offline and use a fixed gains matrix during the Real-Time control of the structure using the steady-state values. This way, the filter becomes much more computationally friendly and is easier to implement in real-time. A Kalman filter with fixed gains is called an Alpha-Beta filter.

## 4.3 LQR controller design

Given a LTI system, we can calculate the state feedback gain matrix  $K$  such that the control law  $u[n] = -Kx[n]$  minimizes the performance index

$$J = \sum_{n=1}^{\infty} (x[n]^T Q x[n] + u[n]^T R u[n]) \quad (50)$$

Where  $Q$  and  $R$  are symmetric and  $Q \geq 0$ ,  $R > 0$ .

$Q$  is used to put weights on the states, meaning any deviation from the desired value is penalized.  $R$  is used to put weight on the input, meaning a high input value is penalized. In the present case, since all the states are decoupled,  $Q$  is a diagonal  $2n \times 2n$  matrix. Since there is only one controllable input,  $R$  is a scalar.

Initially, the goal is to lower the resonant peaks throughout the whole frequency range, therefore all modes must be equally penalized. The  $Q$  matrix will therefore be some constant  $L$  times the identity matrix. The input amplitude need not be overly penalized since the exact actuator dynamics are not yet known, therefore  $R$  is set to 1. The constant  $L$  influences the magnitude of the controller gains, therefore it has to be set so that the resulting control input is about the same magnitude as the disturbance.

## 4.4 $H_{\infty}$ controller design

In order to design an  $H_{\infty}$  controller, the system is setup in a different way as is shown in [Figure 32](#) [15].

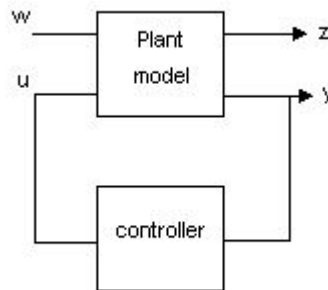


Figure 32 -  $H_{\infty}$  system configuration

The system has two input vectors,  $u$  and  $w$ , as well as two output vectors,  $y$  and  $z$ . The vectors  $u$  and  $y$  are, as before, respectively the control inputs and output

measurements. The input vector  $w$  groups such signals as disturbances, set points or represents modeling errors. The output vector  $z$  contains variables through which the performance of the controller is assessed. These variables must be kept small, in the sense that the design objective is to keep the norm of the transmission  $T_{wz}$  small (closed-loop transfer matrix from  $w$  to  $z$ ). When designing the system, care must be given to the choice of the vectors  $w$  and  $z$  because the specifications of robustness and performance are given in terms of  $T_{wz}$ . These new input and output vectors lead to an augmented state-space representation which combines the system model and models of the weighting functions :

$$\begin{aligned} \dot{x} &= Ax + B_1 w + B_2 u \\ z &= C_1 x + D_{11} w + D_{12} u \\ y &= C_2 x + D_{21} w + D_{22} u \end{aligned} \quad (51)$$

It is necessary at this point to define the  $H_\infty$  -norm of a system. Recall that the  $L_2$ -norm (“regular” norm) of a signal in the frequency domain is defined as :

$$\|\hat{f}\|_2 = \left( \frac{1}{2\pi} \int_{-\infty}^{\infty} \|\hat{f}(j\omega)\|^2 d\omega \right)^{\frac{1}{2}} \quad (52)$$

The norm (or gain) of a system in this case is defined as the maximum ratio of the norm of the input-output to and the norm of the corresponding outputinput. Given a BIBO stable, causal LTI system mapping  $L_2[0,+\infty)$  into  $L_2[0,+\infty)$ , it can be shown [16] that its  $L_2$ -induced norm is defined as :

$$\|H\|_{gain}^2 = \sup_{\|x\|_{L_2} \leq 1} \|h * x\|_{L_2}^2 = \sup_{\omega} \|H(j\omega)\|^2 \quad \text{[note change to norm]} \quad (53)$$

Considering that the inequality holds for a system whose input signal energy is concentrated at the frequency where the maximum amplitude of the frequency response of the system occurs, the  $L_2$ -induced norm of the system is the  $L_\infty$  norm of its frequency response :

$$\|H\|_{gain} = \sup_{\omega} \|H(j\omega)\| = \|H\|_{\infty} \text{ [note change to norm]} \quad (54)$$

When applied to stable systems with finite  $L_{\infty}$  norms ( $H_{\infty}$  space), this norm is also called the  $H_{\infty}$  norm.

When designing an  $H_{\infty}$  controller, the algorithm does not compute the optimal solution but one, which may not be unique, for which  $\|T_{wz}\|_{\infty} < \gamma$ . In this case, the bisection method is used to iterate on the value of  $\gamma$  to approach the optimal  $H_{\infty}$  controller. In order for a solution to exist, the following assumptions must be satisfied [17]:

- (i)  $(A, B_2)$  is stabilizable and  $(C_2, A)$  is detectable
- (ii)  $D_{12}^T D_{12}$  and  $D_{21} D_{21}^T$  are nonsingular (full rank)
- (iii)  $(A, B_1)$  is stabilizable and  $(C_1, A)$  is detectable
- (iv)  $\begin{bmatrix} A - j\omega I & B_2 \\ C_1 & D_{12} \end{bmatrix}$  has full column rank for all  $\omega \in \Re$
- (v)  $\begin{bmatrix} A - j\omega I & B_1 \\ C_2 & D_{21} \end{bmatrix}$  has full row rank for all  $\omega \in \Re$

The Matlab function `hinfsyn` uses the formula described in the Glover and Doyle, 1989, [18] paper to derive a (sub)optimal  $H_{\infty}$  controller when given an augmented state-space system as described above.

## 4.5 Closed-loop system results

### 4.5.1 LQR regulator, collocated actuator

The first case tested represents a perfect scenario and will be used as the benchmark against which the other controllers are tested. In this case, the actuator is collocated with the disturbance at the wheel axle and the controller has access to the true states of the plant (the Kalman filter is not used). The weights applied to each states during the design of the LQR controller are identical to observe which peaks are easy to reduce and which ones require more attention. The weights are also scaled so that the amplitude of the control signal is of the same order of magnitude as the disturbance.

Figure 33 shows the dB attenuation as measured at the b1, x direction sensor while Figure 35 shows the bh, z direction sensor output.

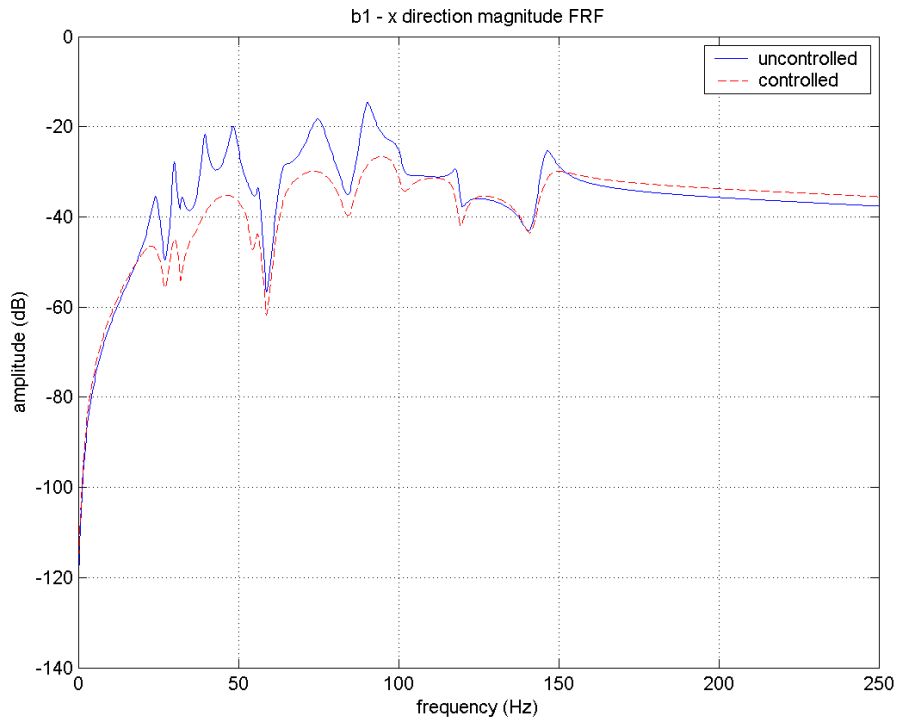


Figure 33 - b1, x direction closed-loop dB attenuation (true states, collocated actuator)

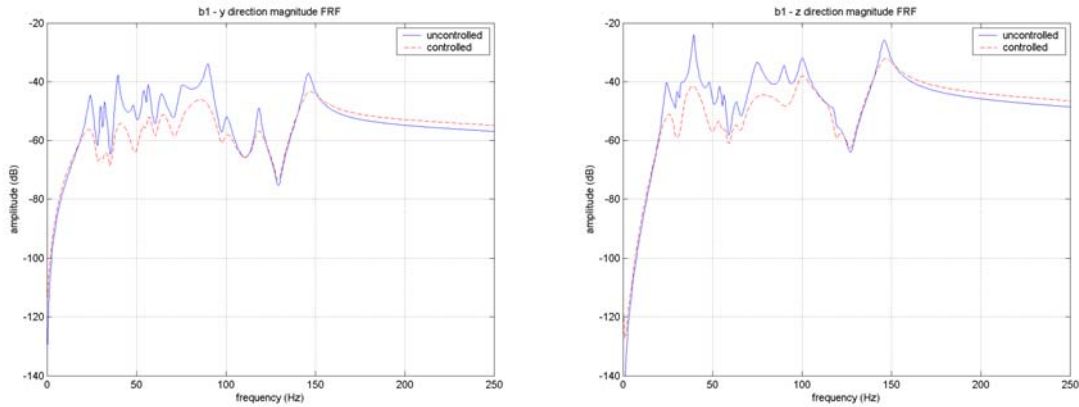


Figure 34 - b1, y (left) and b1, z (right) closed-loop dB attenuation (true states, collocated actuator)

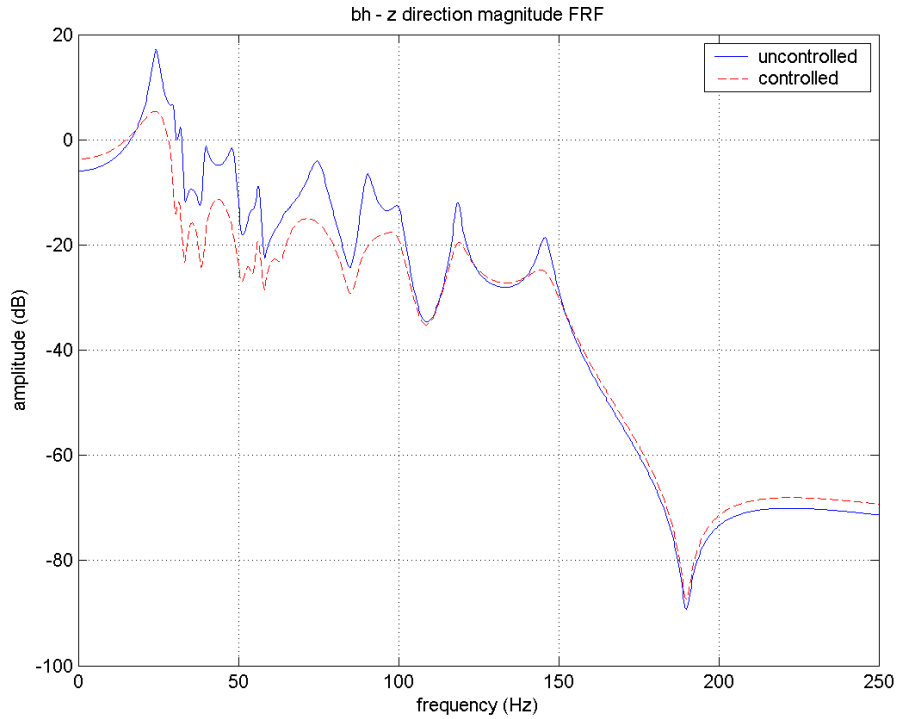


Figure 3535 - bh, z direction closed-loop dB attenuation (true states, collocated actuator)

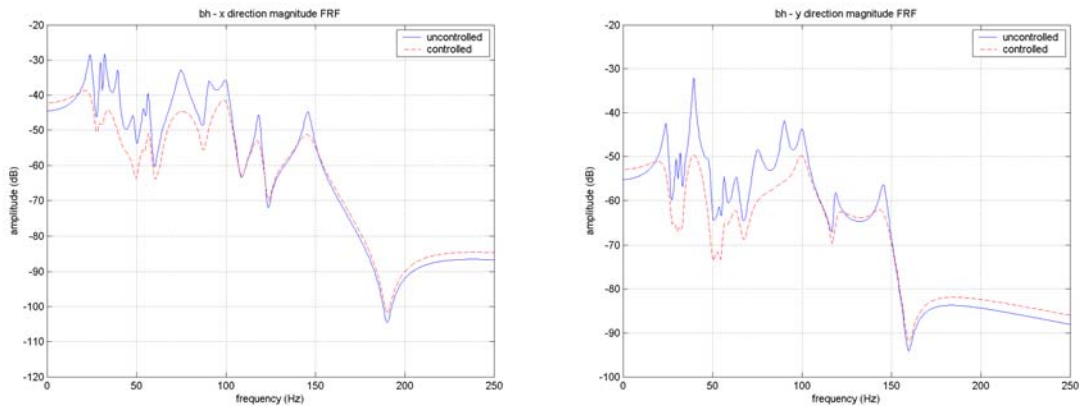
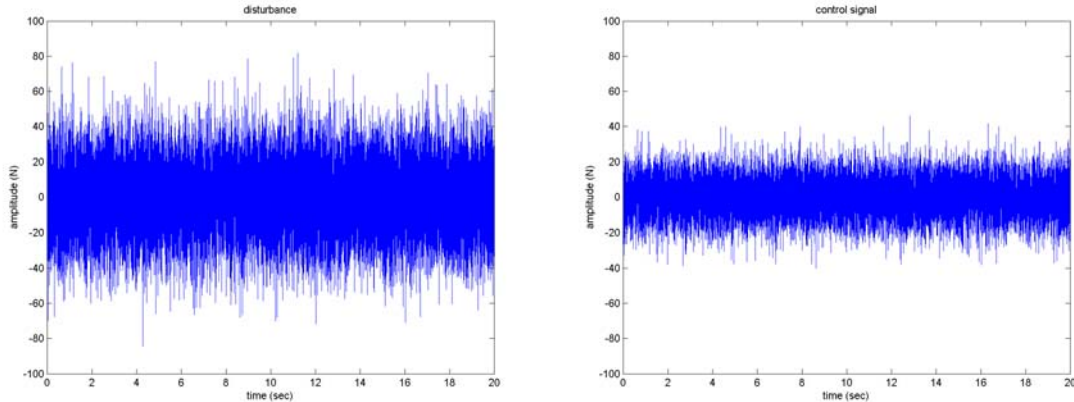


Figure 36 - bh, x (left) and bh, y (right) closed-loop dB attenuation (true states, collocated actuator)

As can be seen, an attenuation of 12-16 dB is attained for the modes below 100 Hz where all of the resonance peaks have disappeared, whereas an attenuation of only about 5-7 dB is achieved for the modes above 100 Hz.

Figure 37 shows the disturbance amplitude and the control signal amplitude for the LQR feedback controller. The disturbance is of the same magnitude and spectrum (white noise) as the disturbance used on the experimental test bench to acquire the FRF data. It can be observed that the control signal is of the same order of magnitude. Hence, it is well within the capabilities of the actuator, since the shaker used in the real system to simulate the actuator will be identical to the one used to input the disturbance.



**Figure 37 – Disturbance (left) and control signal (right) amplitude**

As mentioned earlier, the real controller will not have access to the true states but only to the estimated states as reconstructed by the Kalman filter. Furthermore, some noise is added to the output sensor signals. Therefore, a loss of performance is to be expected because of the possible discrepancy between the real and estimated states during the simulation. The following figures show, for the same  $b_1 - x$  and  $b_h - z$  sensors, the attenuation of vibrations in a the system with the Kalman filter in the loop.

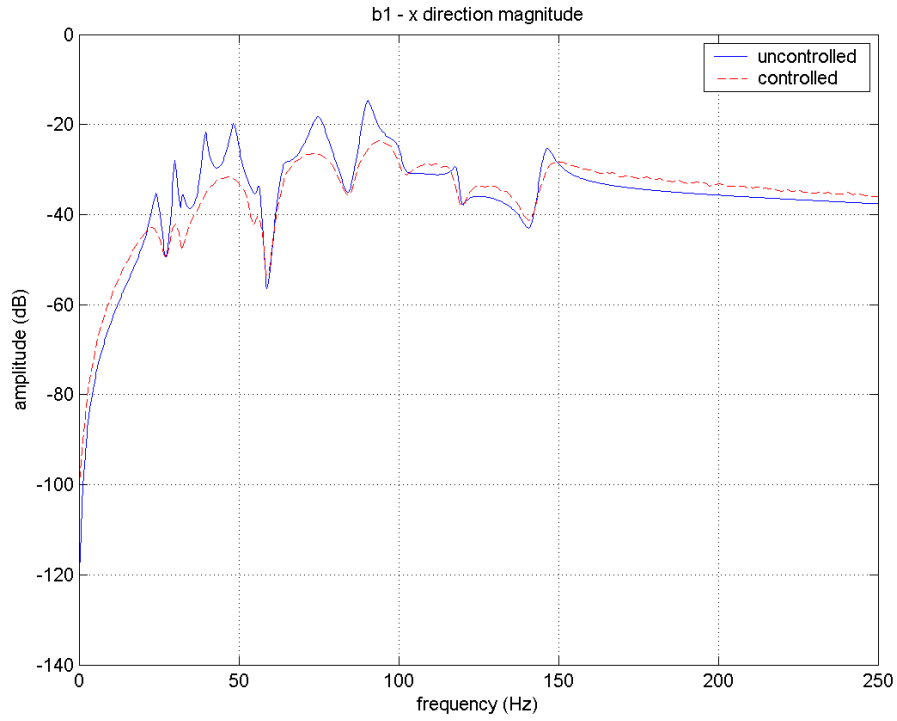


Figure 3838 – b1, x direction closed-loop dB attenuation (estimated states, collocated actuator)

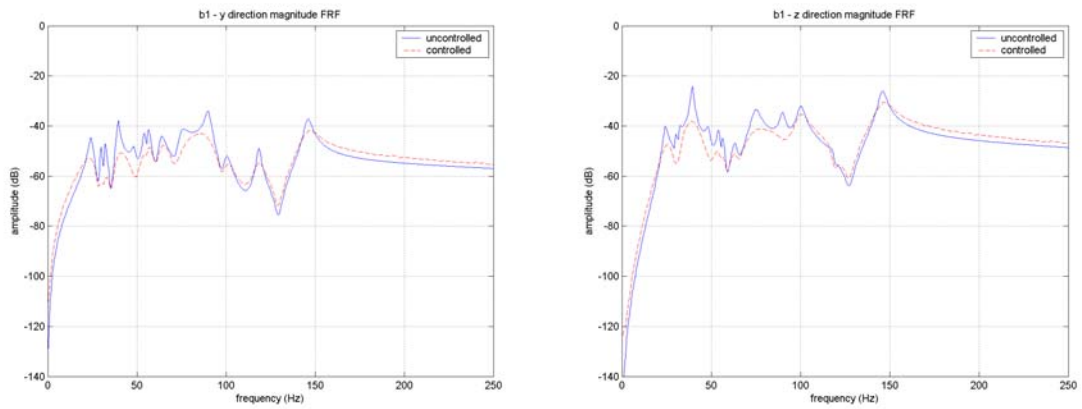


Figure 3939 – b1, y (left) and b1, z (right) closed-loop dB attenuation (estimated states, collocated actuator)

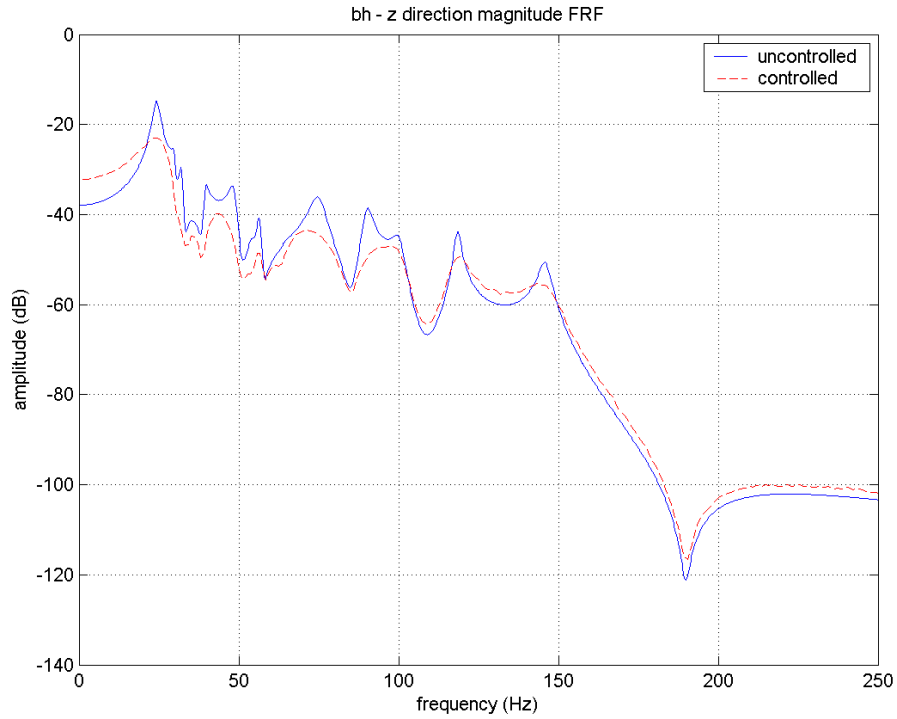


Figure 4040 - bh, z direction closed-loop dB attenuation (estimated states, collocated actuator)

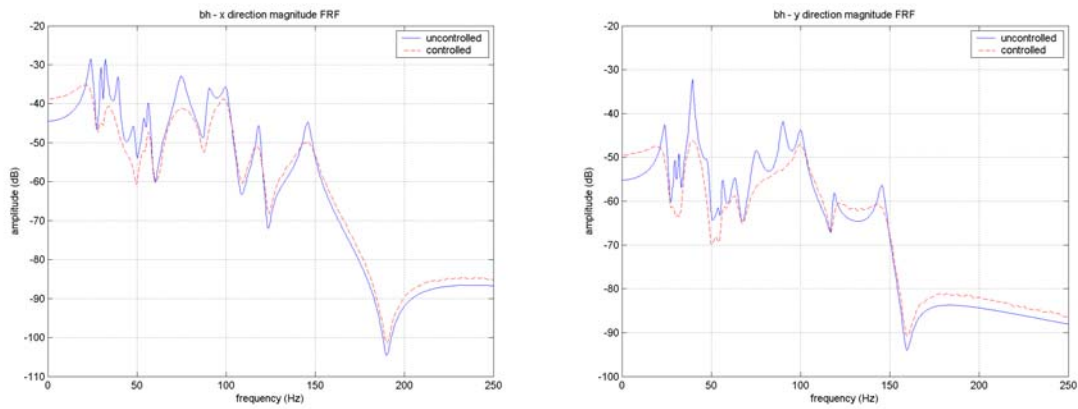


Figure 4144 - bh, x (left) and bh, y (right) closed-loop dB attenuation (estimated states, collocated actuator)

As expected, there is a slight drop in the performance of the controller following the addition of the Kalman filter of about 1-2 dB for the lower frequency modes. The performance loss is more noticeable for the high-frequency modes (especially modes 12

and 13). Note that the behavior of the controller at frequencies below 20 Hz is not consequential, since the model is highly uncertain at these frequencies.

Given that the high-frequency peaks are less attenuated than those of lower frequency, a second LQR controller is designed with heavier weights on the higher frequency modes, and lower weights on the lower frequency modes. The resulting FRFs are shown in the following figures. The Kalman filter is still used, and the actuator is collocated with the disturbance.

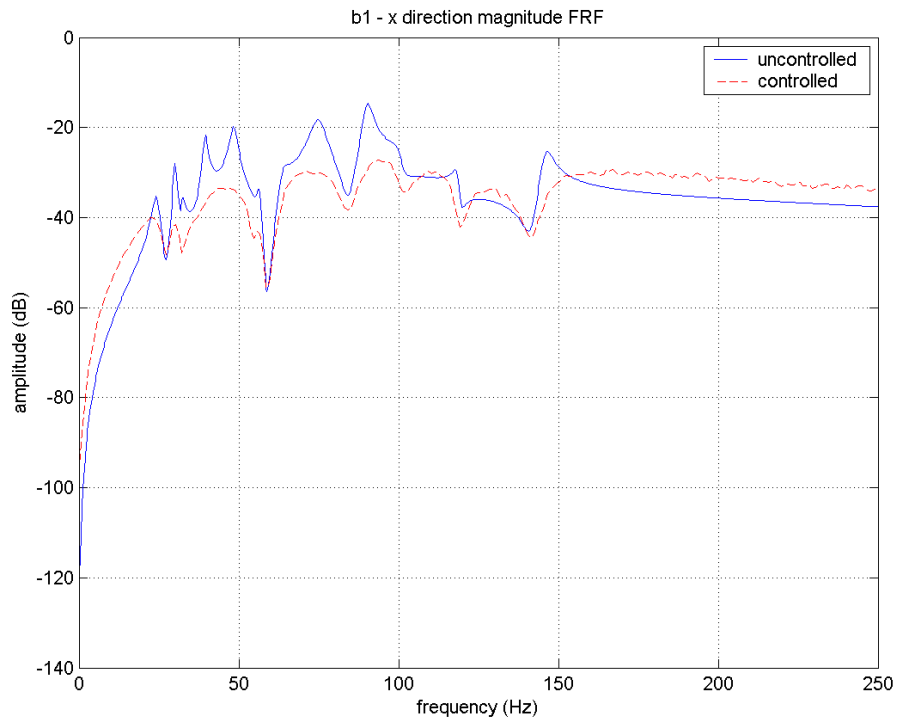


Figure 4242 - b1, x direction FRF with emphasis on reducing high-frequency peaks

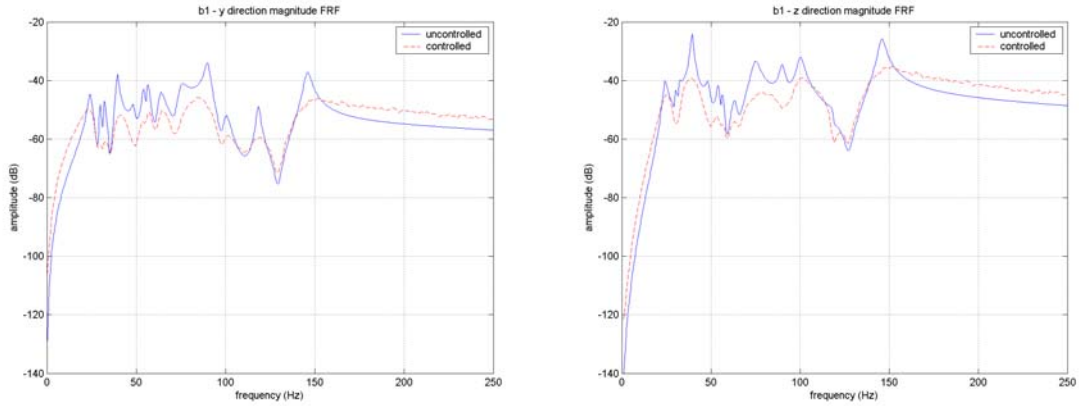


Figure 4343 - b1, y (left) and b1, z (right) FRF with emphasis on reducing high-frequency peaks

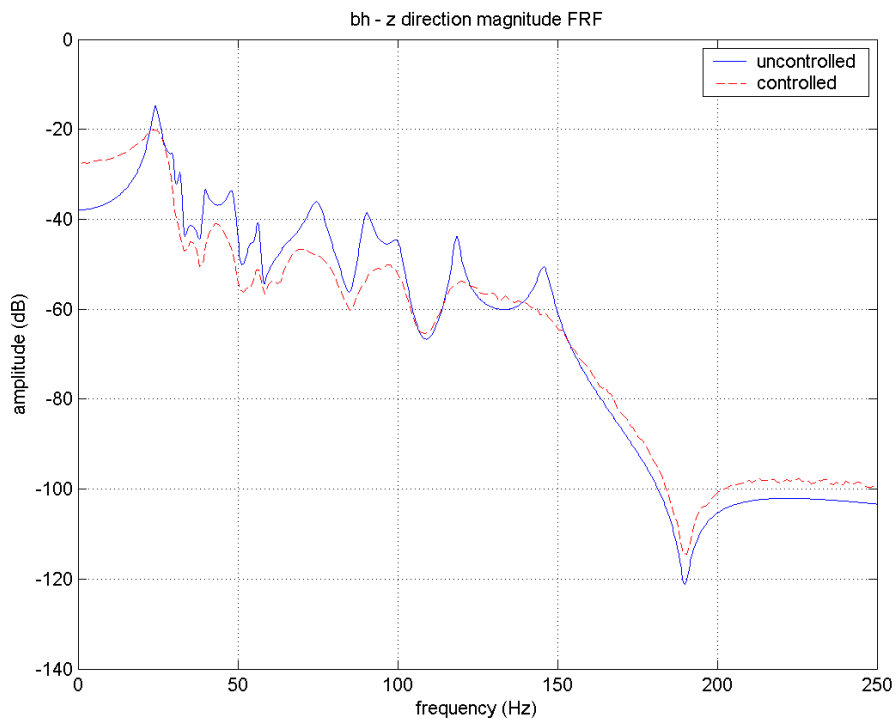
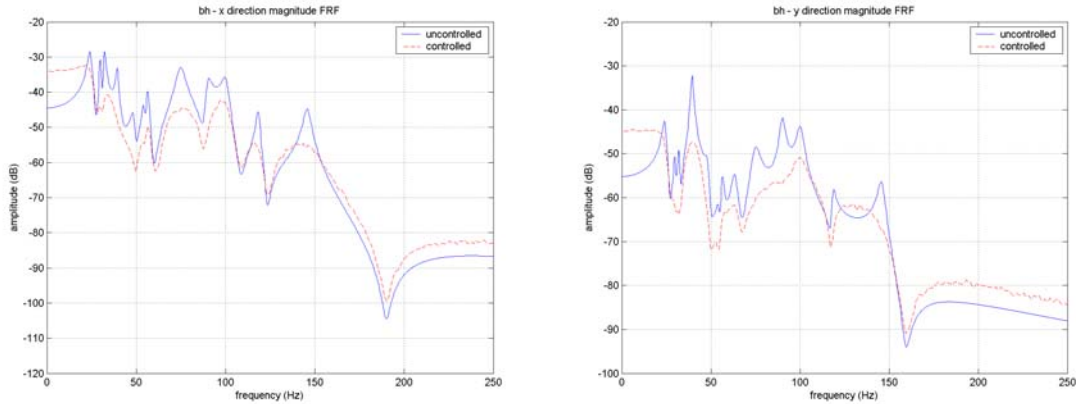


Figure 4444 - bh, z direction FRF with emphasis on reducing high-frequency peaks



**Figure 4545 - bh, x (left) and bh, y (right) FRF with emphasis on reducing high-frequency peaks**

From the above pictures, a slight decrease of about 2-3 dB in the magnitude of the higher frequency peaks can be observed. There is, however, as small decrease in the performance of the controller at lower frequencies. To achieve a higher attenuation of the high frequency peaks without losing performance at lower frequencies, the control signal would have to be of higher amplitude. It is therefore a tradeoff between actuator amplitude and attenuation of the resonance peaks, with the weighting matrix of the LQR regulator influencing which frequencies are more attenuated.

## 4.5.2 LQR regulator, non-collocated actuator

The actuator in this case is placed under the suspension bottom attachment points and acts in the z direction. The model developed in section 3.6, with a new B matrix, must therefore be used. However, as is demonstrated in ~~Figure 46~~Figure 46, the new actuator location does not have as much effect on the structure's vibrations, for an equivalent amplitude, as when placed at the wheel axle. The full line represents the output of the sensor placed bh, in the z direction when the actuator is positioned at the wheel axle. The dotted line represents the output from the same sensor and with the same amplitude white-noise input signal, but with the actuator positioned under the base of the suspension. It is easily observable that the amplitude of the vibrations recorded are

several dB lower when the actuator is located at the base of the suspension than when the actuator is located at the wheel axle. Similarly, the actuator in this position has much less effect in the x and y directions as compared to acting at the wheel axle. This lack of influence is especially noticeable for the mid frequencies. Only modes 1 and 13 seem to be excited to almost the same level independently of the placement of the actuator.

Considering the lack of influence of the new actuator location, a much poorer performance is to be expected as compared to when the actuator is collocated with the disturbance.

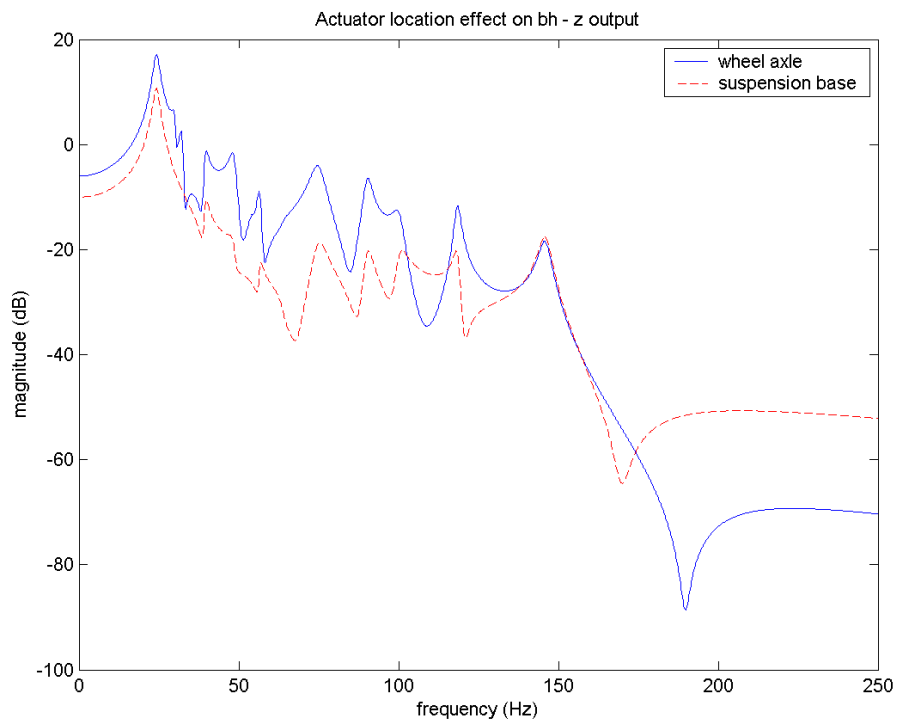


**Figure 4646 – Comparison of the effect of actuator placement, bh – z direction sensor**

The following figures show the vibration attenuation in dB as measured at multiple sensor locations sensors when the actuator is placed at the base of the suspension. All states in this case are weighted equally when designing the LQR regulator.

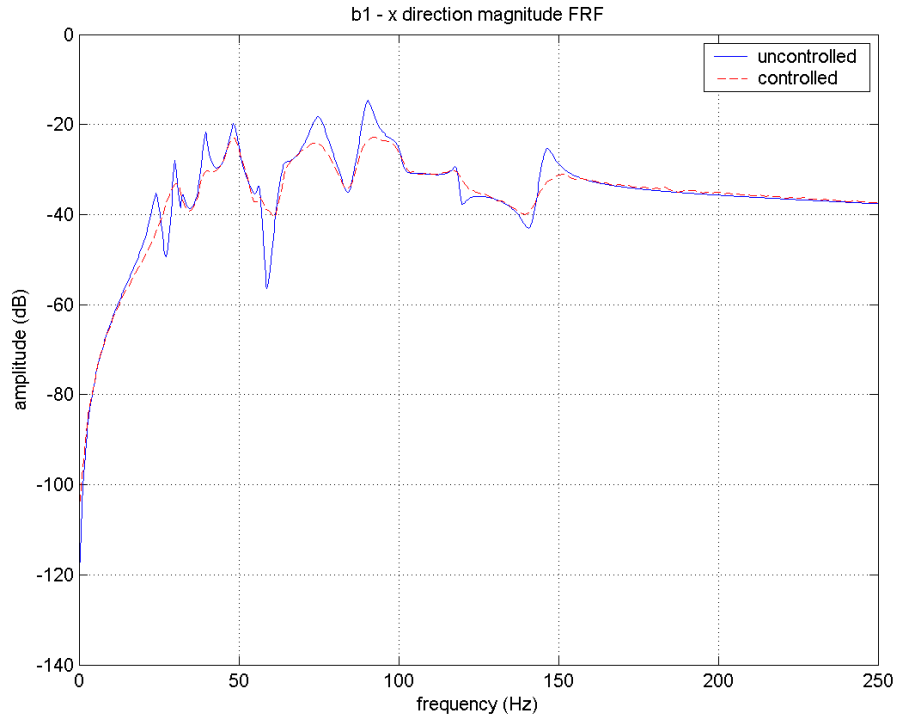


Figure 4747 – b1, x direction closed-loop dB attenuation (estimated states, non-collocated actuator)

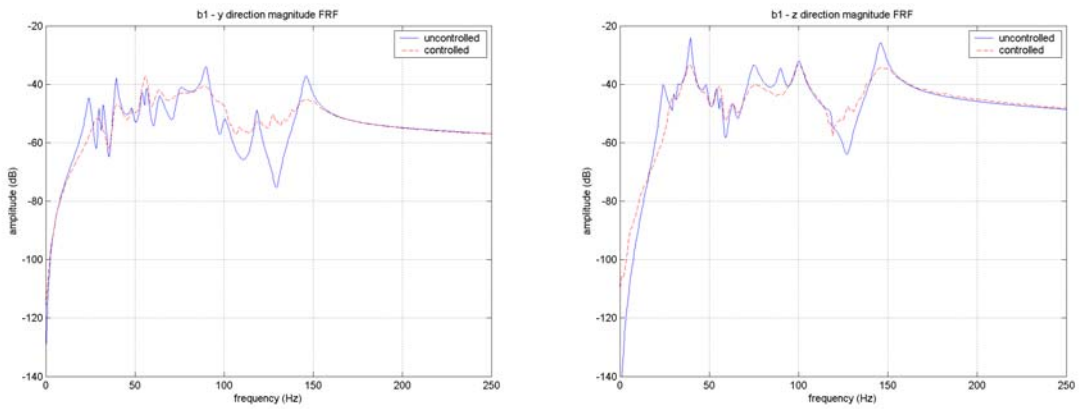


Figure 4848 – b1, y (left) and b1,z (right) closed-loop dB attenuation (estimated states, non-collocated actuator)

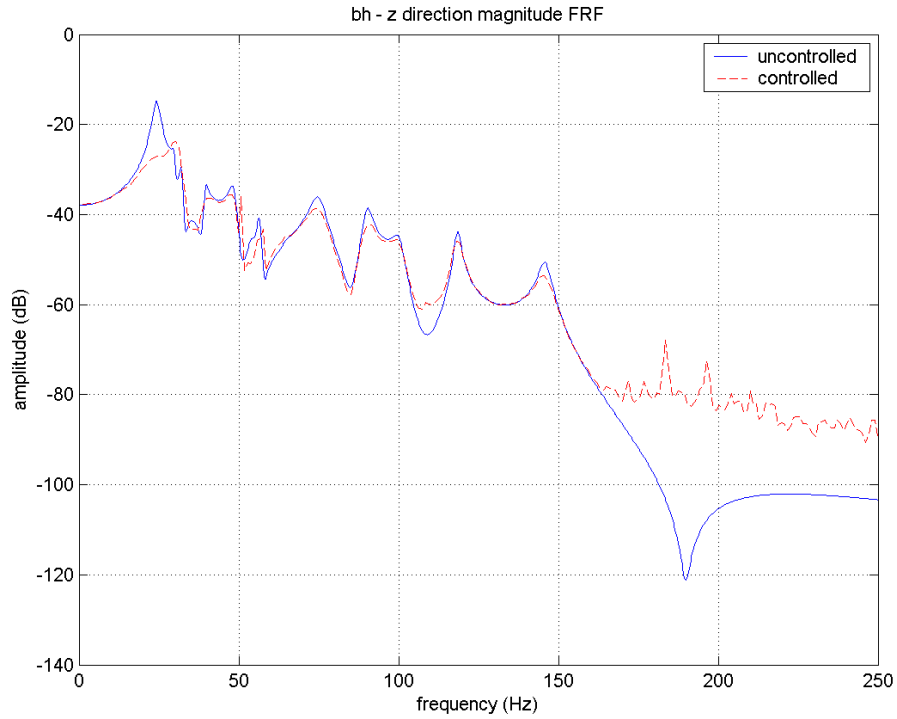


Figure 4949 – bh, z direction closed-loop dB attenuation (estimated states, non-collocated actuator)

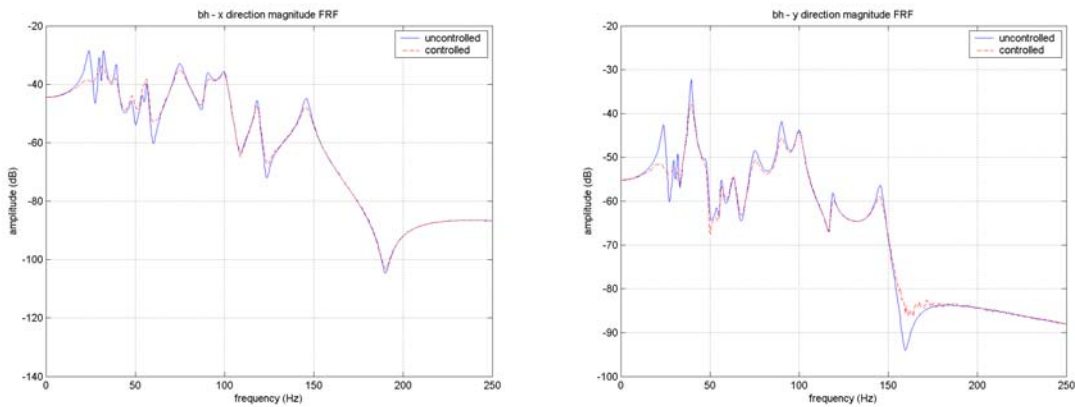


Figure 5050 – bh, x (left) and bh, y (right) closed-loop dB attenuation (estimated states, non-collocated actuator)

As expected, the first mode is the most attenuated because the actuator has ~~as-a~~ strong influence over it. However, when positioned under the base of the suspension, it has very little effects on most of the remaining resonance modes. Therefore, using a

control signal of the same magnitude as when the actuator is collocated with the disturbance, the resulting attenuation of the peaks is very small. It would therefore be necessary to increase the gains of the controller significantly to achieve the same performance as a collocated actuator. This can result in a control signal that is too high and saturates the actuator. Another option is to find a position on the suspension where the actuator has as much effect, or more, on the vibration modes as when positioned at the wheel axle. If attenuation of a specific vibration mode is desired, the best solution is to identify among all the possible actuator locations the one where this mode is the most excited. By placing the actuator at this location, the biggest attenuation of this mode can be achieved with an equivalent control signal amplitude.

### 4.5.3 $H_\infty$ controller, collocated actuator

The design of an  $H_\infty$  controller requires the design of an augmented system matrix  $P$  of the form

$$P = \left[ \begin{array}{c|cc} A & B_1 & B_2 \\ \hline C_1 & D_{11} & D_{12} \\ C_2 & D_{21} & D_{22} \end{array} \right] \quad \text{[note added lines to denote a transfer matrix} \quad (55)$$

instead of a constant matrix. standard notation]

$B_1$  is set so as to give a 30% uncertainty on the states (value based on the addition of the errors caused by the experimental data acquisition and curve fit process) as well as the input gains matrix of the disturbance, which is in this case collocated with the actuator.  $C_1$  is the identity matrix to give equal weight to all 26 states of the system. The matrices  $A$ ,  $B_2$  and  $C_2$  are the system matrices as defined previously.  $D_{12}$  and  $D_{21}$  are set to very small values to satisfy the assumptions for a solution to exist. [usually A is also augmented with the dynamics of the weighting functions, but I guess you used a constant weight on w, which is OK]

The figures below show the results obtained with a closed-loop state-feedback  $H_\infty$  controller on the system. The Kalman filter is used to provide estimates of the 26 states to

the controller. The controller system outputs, during a simulation, a control signal which is of slightly smaller amplitude than the LQR generated control signal.

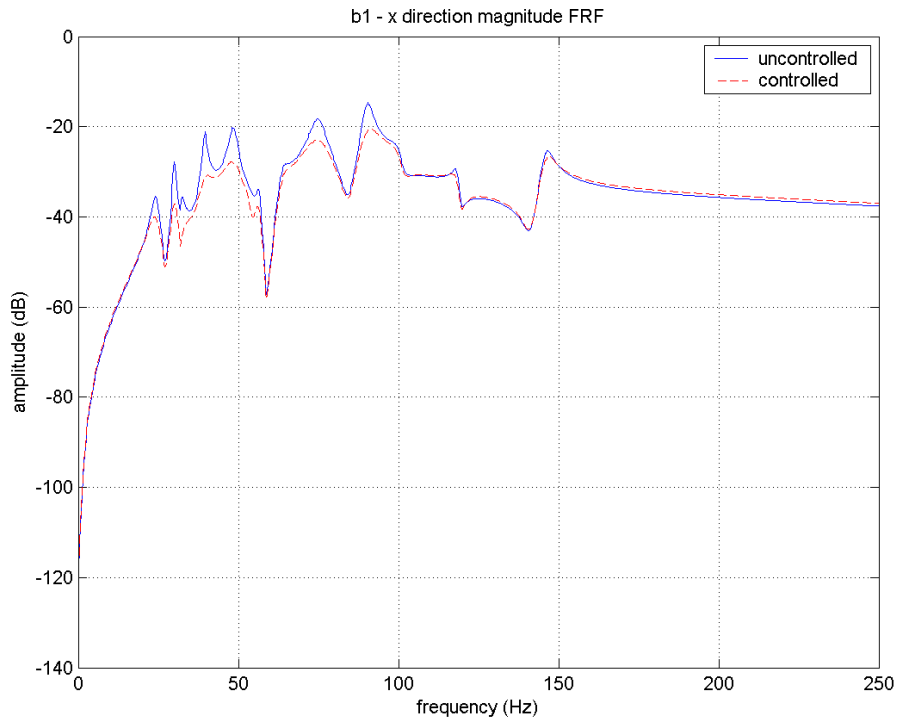


Figure 5154 – b1, x direction closed-loop dB attenuation ( $H_\infty$  controller)

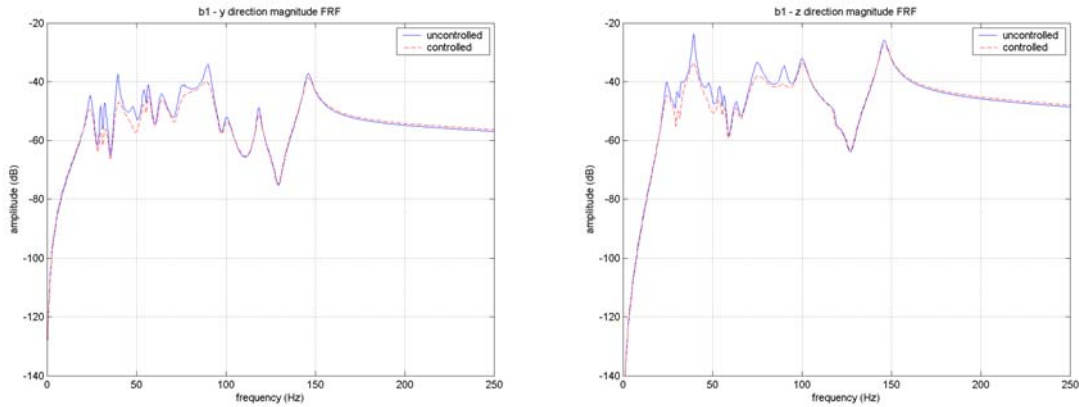


Figure 5252 – b1, y (left) and b1, z (right) direction closed-loop dB attenuation ( $H_\infty$  controller)

For the lower base of the suspension sensors, an attenuation of between 5-9 dB can be observed on the resonance peaks below 100 Hz using the  $H_\infty$  controller.

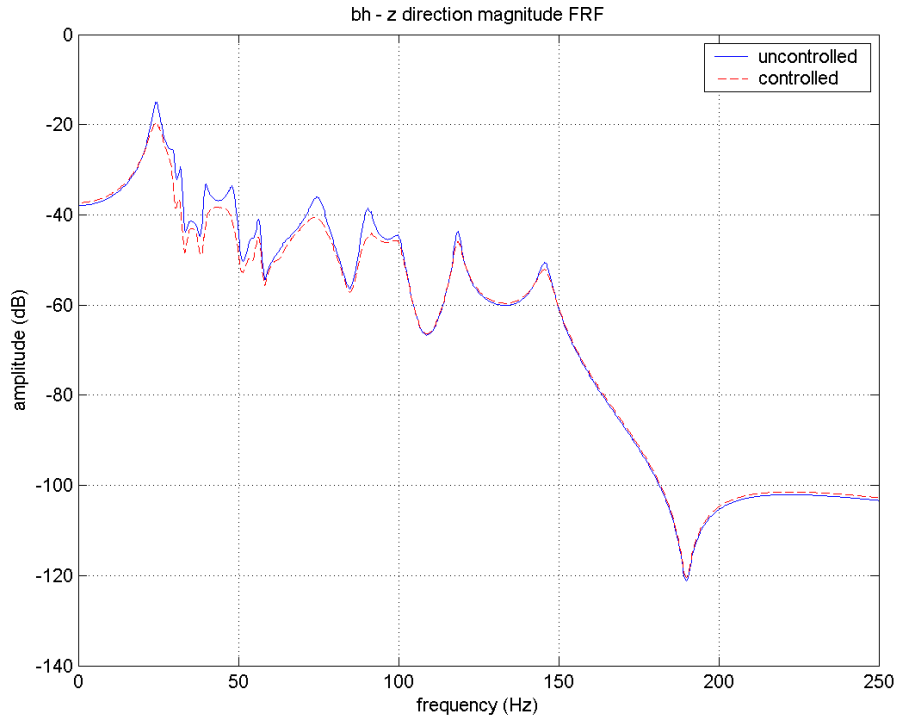


Figure 5353 - bh, z direction closed-loop dB attenuation ( $H_\infty$  controller)

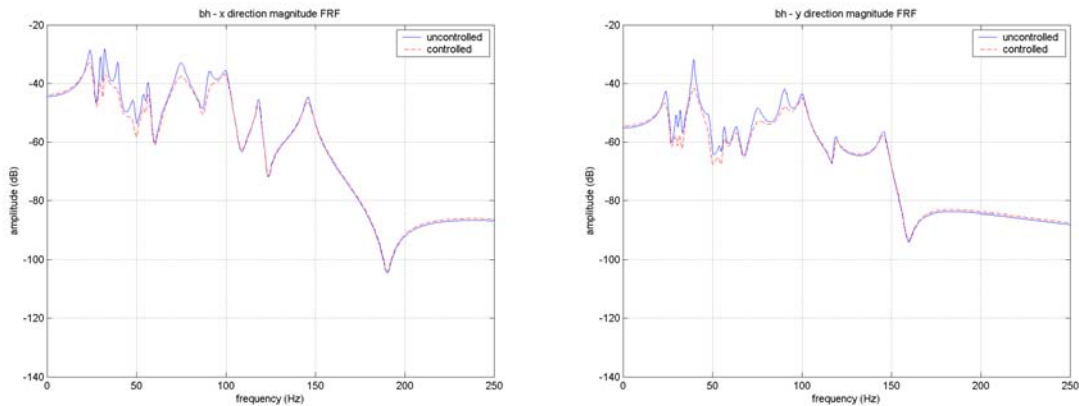


Figure 5454 - bh, x (left) and bh, y (right) direction closed-loop dB attenuation ( $H_\infty$  controller)

Similarly, the head sensors register an attenuation of the peaks below 100 Hz of about 5-8 dB. While this performance is lower than that of the LRQ, the  $H_\infty$  controller is very robust and will maintain its performance on the real system despite modelling errors, as is shown on the following figures. A new model is derived with random variations introduced on the modal parameters. The variations are of up to 10% on the modal

frequencies and 40% on the damping ratios. The same controller as has been applied to the previous system is applied to this “randomized” model to see if the controller retains its performance.

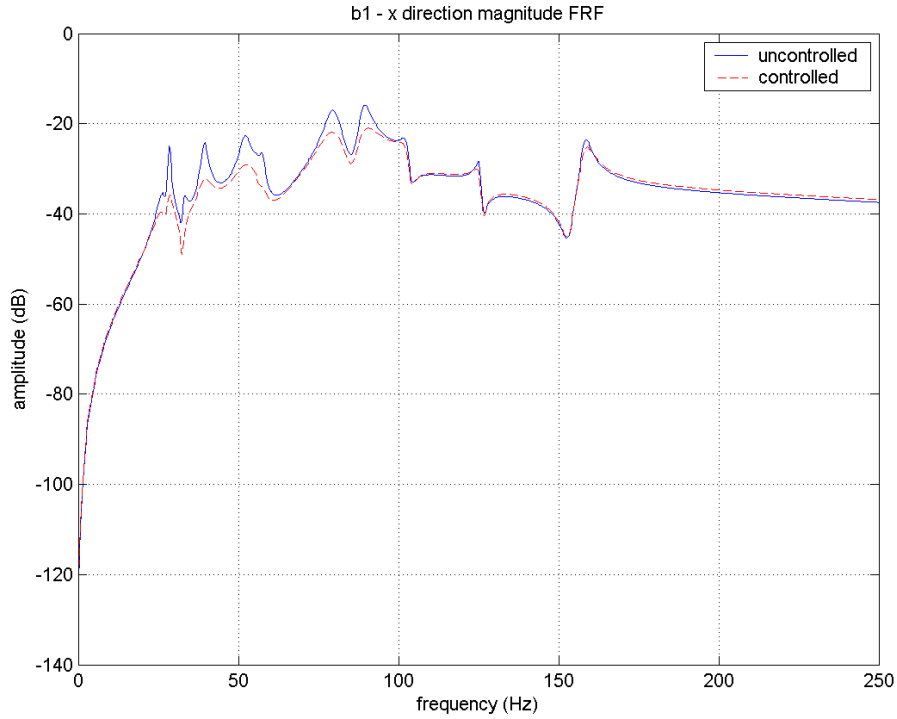


Figure 5555 – b1, x direction closed-loop dB attenuation on randomized model ( $H_\infty$  controller)

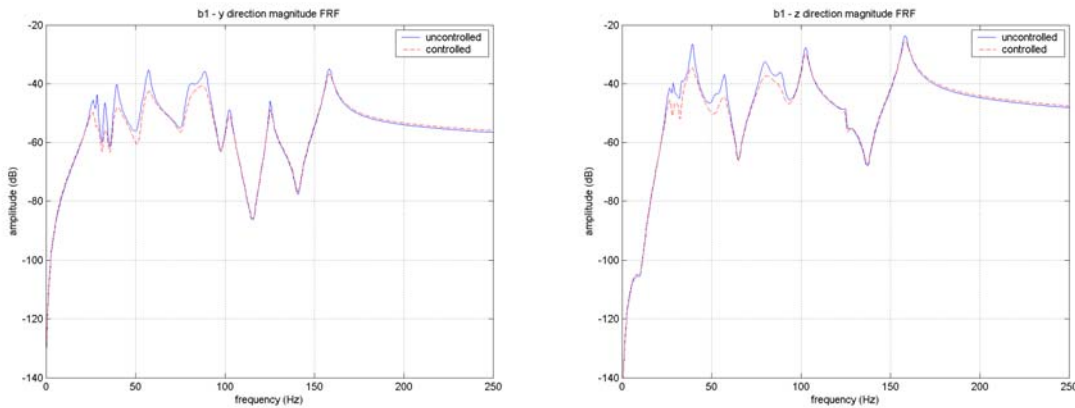


Figure 5656 – b1, y (left) and b1, z (right) direction closed-loop dB attenuation on randomized model ( $H_\infty$  controller)

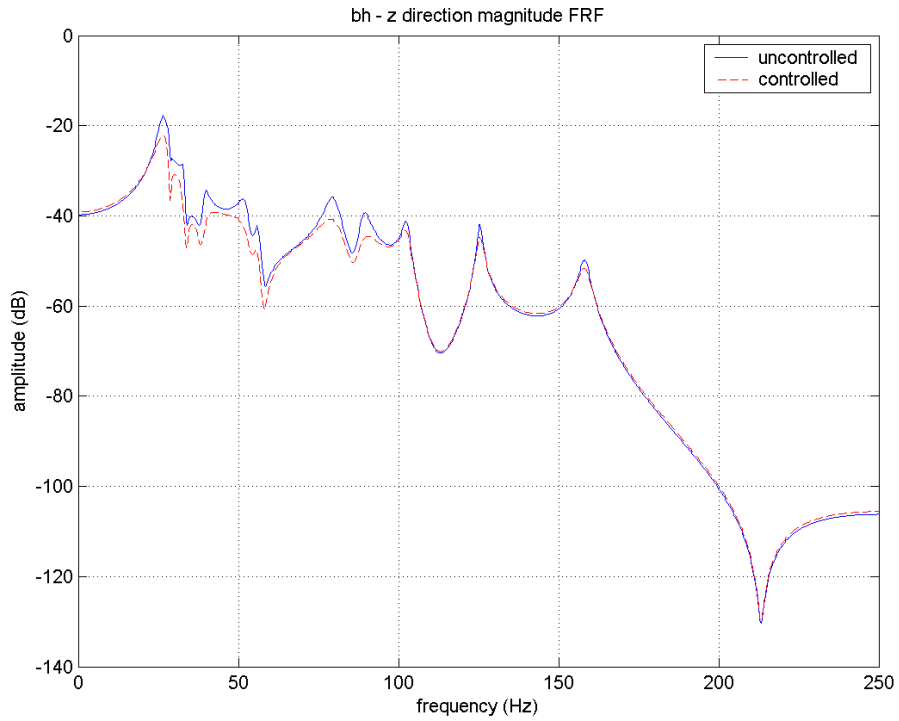


Figure 5757 – bh, z direction closed-loop dB attenuation on randomized model ( $H_\infty$  controller)

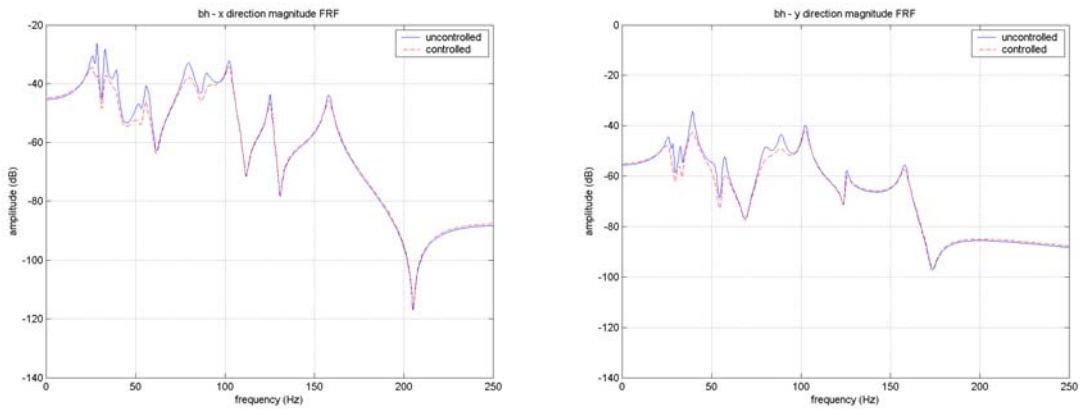


Figure 5858 – bh, x (left) and bh, y (right) direction closed-loop dB attenuation on randomized model ( $H_\infty$  controller)

As can easily be observed on the above figures, despite a model that is fairly different ~~than from~~ the one used to derive the controller, the performance of the  $H_\infty$  controller remains as good as when it was applied to the original model.

Using these results, the  $H_\infty$  controller can be applied to the real system with the confidence of knowing that it will yield a reasonable level of performance even if the real system differs from the model because of uncertainties in the modeling process.

---

# 5 Conclusion

## 5.1 Summary

The model of a  $\frac{1}{4}$  car suspension derived in this thesis is obtained by fitting modal parameters to experimental data obtained on a test bench. ~~13~~Thirteen DOFs are identified in the frequency range 20Hz to 160Hz, as the resonance peaks in this frequency range are the most likely to induce noise-generating vibrations in the frame of an automobile. A 26<sup>th</sup> order state-space realization of the model is derived.

In an effort to reduce the vibrations transmitted to the frame of the vehicle, an actuator, collocated with the disturbance at the wheel axle, is added to the system. A state-feedback controller drives the actuator. A Kalman filter is used to reconstruct the states based on the inputs to the system and data from 15 force and acceleration sensors located at the suspension attachment points.

The first controller design technique evaluated is an LQR regulator. By weighting equally each state and using a control signal of the same order of magnitude as the disturbance, an attenuation of 10-12 dB is achieved through simulation for the modes below 100 Hz, while the higher frequency modes are attenuated by 5 dB. In order to increase performance at high frequency, the states corresponding to the higher modes are weighted more heavily when designing the controller. While keeping the control signal to the same amplitude, the resulting attenuation of the high frequency peaks increases by several dB (depending on the sensor output) while the performance at lower frequency decreases slightly.

A different location for the actuator is evaluated. Instead of being collocated with the disturbance, the actuator is positioned under the base of the suspension. However, this location has less influence on most resonance modes, therefore a decrease in performance over the collocated actuator is to be expected for a control signal of equivalent amplitude. Simulation results indicate that attenuation for most modes is about 2-5 dB.

While every effort has been made to model the  $\frac{1}{4}$  car suspension as accurately as possible, it is impossible to obtain a 100% accurate model. It is therefore important to know that the controller will perform on the real system even if it differs from the model. Keeping this in mind, an  $H_\infty$  controller is designed to give an acceptable level of performance while being robust to variations in the system. The controller is designed using an augmented state-space model accounting for the disturbances that will be present on the real system. The resulting controller, while not as efficient as the LQR regulator, gives very good performance on the model of the suspension as well as on models that have been modified to simulate the real system.

## 5.2 Future work

The next logical step in the current project is to test the different control algorithms on the actual experimental test bench to assess the real-world performance of the work done in simulation. A continued study of the placement of the actuator will also be beneficial. As seen, the choice of the placement of the actuator can have a great impact on the response of the structure. It has been shown that when the actuator is placed at the base of the suspension, it has a much lesser impact on the resonance modes than when positioned at the wheel axle. It will therefore be necessary to test several potential positions for the actuators to determine which one is the most effective.

The model currently used is derived from experimental data. The development of a Finite Element Model of the suspension will enable the correlation of the experimental data to the FEM through such method as the Modal Assurance Criterion (MAC). This process ensures the validity of both the FEM and the experimental model while increasing confidence in both.

Developing a structural-acoustic FEM of a complete automobile will also take the project further. The global aim being to reduce the noise level inside the passenger compartment of the car, the knowledge of which frequencies produce the most noise will

enable the tuning of the controller to reduce specifically those noise-generating frequencies. Furthermore, using the FEM in the simulation will allow the use of microphones placed at strategic emplacements in the passenger compartment to be used as the feedback signal to the controller. The ability to control directly the noise level will therefore improve the controller's performance.

It will also be useful to characterize the disturbance that will be encountered by the real system to be able to simulate the system under the most realistic circumstances as possible. By having a good idea of the amplitude and spectrum of the disturbances, it will be easier to tune the controller.

The actuators used on the test bench are wide-spectrum high power shakers. However, the actuators that will be used on the real system will have a much more limited bandwidth and maximal amplitude. This is due to cost, physical space and power constraints. Therefore, the actuators chosen will have to be tuned to attenuate the frequencies identified in the FEM as producing the most noise. The controller will have also to be tuned accordingly, by assigning heavier weights to these frequencies.

And eventually, the only sound heard in an automobile will be your better half telling you to slow down. (this sentence might not make it to the final version). (I would keep it! :-)

## REFERENCES

- [1] L. Hermans and H. Van Der Auweraer, *Modal Testing and Analysis of Structures Under Operational Conditions : Industrial Applications*. Mechanical Systems and Signal Processing **13**(2), 193-216, 1999.
- [2] S.H. Kim, J.M. Lee and M.H. Sung, *Structural-Acoustic Modal Coupling Analysis and Application to Noise Reduction in a Vehicle Passenger Compartment*. Journal of Sound and Vibration **225**(5), 989-999, 1999.
- [3] U. Stobener and L. Gaul, *Active vibration control of a car body based on experimentally evaluated modal parameters*. Mechanical Systems and Signal Processing **15**(1), 173-188, 2001.
- [4] I.N. Kar, K. Seto and F. Doi, *Multimode Vibration Control of a Flexible Structure Using  $H_\infty$ -Based Robust Control*. IEEE/ASME Transactions on Mechatronics, vol 5, no 1, 23-31, 2000.
- [5] S.J. Elliott, *Active Control of Structure-Borne Noise*, Journal of Sound and Vibrations **177**(5), 651-673, 1994
- [6] Papier Hugo
- [7] D. Ewings, *Modal Testing: Theory, Practice and Application*. Research Study Press LTD, 2000.
- [8] D. Ewings, *Modal testing : Theory and practice*. Research Studies Press LTD, 1984.
- [9] J. He and Z-F. Fu, *Modal Analysis*. Oxford: Butterworth-Heinemann, 2001.
- [10] Curve fitting documentation
- [11] W. Gawronski, *Balanced Control of Flexible Structures*. London: Springer, 1996.
- [12] W. Gawronski, *Dynamics and Control of Structures*. New York: Springer, 1998.
- [13] SDT doc
- [14] L39 SS2
- [15] Belanger book
- [16] 304-501 L9

- [17] The Mathworks Inc, *Mu-Analysis and Synthesis Toolbox User's Guide*.
- [18] J.C. Doyle, K. Glover, P.O. Khargonekhar and B.A. Francis, *State Space Solutions to Standard  $H_2$  and  $H_\infty$  Control Problems*. IEEE Transactions on Automatic Control, vol 34, 831-847, 1989.